



POLITECNICO DI TORINO

Department of Electronics and Telecommunications

Master's Degree Course in Electronic Engineering

Master's Degree Thesis

**Analysis of Diffraction Gratings
of finite extent**

Supervisors

Prof. Renato ORTA

Dr. Alberto TIBALDI

Prof. Guido PERRONE

Candidate

Fabio BERTUCCIO

October 2018

Contents

Introduction	1
1 Introduction	1
2 Foundations of the Rigorous Coupled-Wave Analysis applied to diffraction gratings	5
2.1 Formulation of the scattering problem	6
2.1.1 Junction Problem	9
2.1.2 Reconstruction of the dielectric profile	16
2.2 MMT - Focus on Projection matrices	20
3 Simulations related to the diffraction grating behaviour	25
3.1 Grating excited by a plane wave	26
3.2 Grating excited by a Gaussian beam	35
4 Conclusions	51

Introduction

The realization of the first diffraction grating dates back to 1786 [1], when the astronomer David Rittenhouse realized its prototype by using hairs bounded to a couple of screws with a very narrow pitch. Nevertheless, some scientists considered the physicist Joseph Ritter von Fraunhofer as the father of such structure[2] for his contribution related to the development of this instrument in 1821, after that he invented really important optical instruments such as achromatic objective lenses and spectroscopes (in which diffraction grating has been employed).

During the years, diffraction gratings played important roles in several applications concerning electronics. Just to make an example, this device is employed in scatterometry, i.e. a technique used to verify the correctness of critical dimensions of the semiconductor wafers after the photolithography process[3]. The role of diffraction grating here is to diffract the suitable components (in terms of wavelengths) of a light source able to penetrate in the semiconductor chip, towards the target layer. Reflected light components provided by the sample layer are caught by photo detectors in order to check if the produced wafer complies with the critical dimensions. This kind of proof allows to calibrate the photolithography process for the successive operations.

Although the physics behind the diffraction grating have been studied for about two centuries, it is quite hard to simulate the behaviour of such device due to its finiteness. There are already existent numerical methods such as the finite difference time domain (FDTD), which uses discretized Maxwell's equations to reconstruct the electric fields. Nevertheless, FDTD requires big computational resources for precise and accurate simulations. For this reason, a different approach concerned to modal methods has been analysed in this thesis. In particular, the idea is to simulate a periodic structure behaving like a finite one, reconstructing each period with a central grating and a long spacing layer of each its side, simulating the device finiteness. As future work, the length of spacing layers could be reduced by introducing some

”absorption conditions” [4] in order to make negligible the field contribution at the unit cell boundaries.

However, the first step of this work concerns the study of a diffraction grating of infinite extent. The semi-analytic method of rigorous coupled-wave analysis (RCWA) is used and it is based on the development of Floquet modes employed to describe the behaviour of a periodic dielectric profile. All theory about RCWA and explanation of the mode matching technique (MMT) have been carried out in Chapter 2.

As first approximation, the diffraction grating is considered illuminated by a plane wave. In this case, it is possible to directly analyse the scattering parameters in the simulation part (Chapter 3), since the scattering matrix describe, by definition, the scattered behaviour of a dielectric structure stimulated by a plane wave.

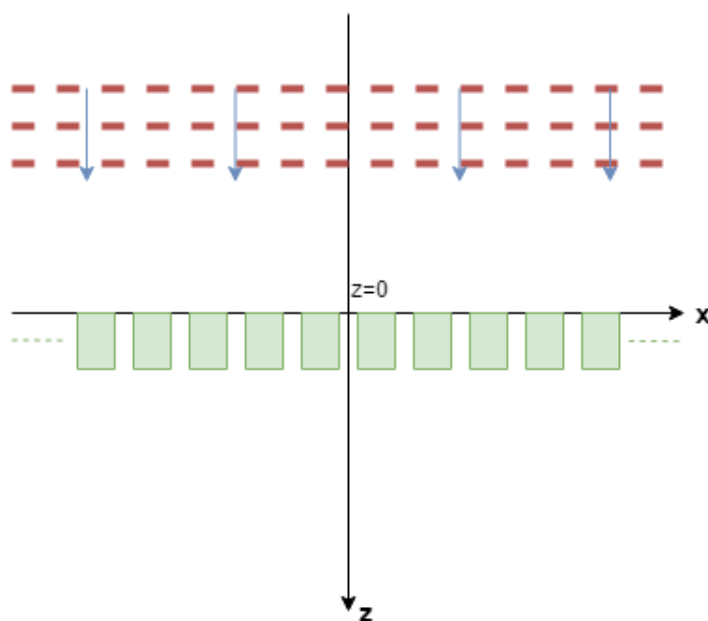


Figure 1.1: Example of diffraction grating with infinite extents illuminated by a plane wave incising normally.

Scattering parameters have been firstly theoretically expressed in section 2.1.1, then they have been numerically calculated by means a MATLAB® function. Floquet modes represent a basis for the electromagnetic fields in the homogeneous half-spaces, while the ”grating modes” (even called phase-shift wall waveguide (PSWW) modes) are defined by means a linear combination of the aforementioned modes with coefficients related to the eigenvalue problem described in section 2.1.

An useful exercise aimed to understand how the periodic cell can be modified has been done in section 3.1. The period of the diffraction grating of infinite extent is initially considered to be composed by a single bar per unit cell. Then, referring to

the same dielectric structure of before, the period taken into account groups now three bars and in section 3.1 it is shown how scattering parameters fit the previous ones properly changing the number of considered Floquet modes in the MATLAB® script. Furthermore, diffraction grating of infinite extent has been studied considering a Gaussian Beam as incident wave as well, which is a more realistic source than a plane wave having infinitely extended wave fronts. Gaussian Beam is characterized by a beam waist and the simulation regarding this kind of incident wave has been developed in section 3.2. Such a wave can be summarized as a sum of several plane waves having each one a different incident angle with respect to the others. At the main value of the Gaussian beam, the whole set of plane waves result in phase, having a constructive contribution. Far from the main value of the bell curve, plane waves interfere one to each others in a destructive way providing a very small field intensity, i.e. producing the so called "tails" of the Gaussian curve.

The fact to describe this kind of incident wave by means a summation of plane waves involves the huge advantage to use again RCWA, performing several times the respective MATLAB® script for each incident angle ϑ . Once the grating with infinite extent is simulated, a model which is closer to a diffraction grating of finite extent has been realized: using RCWA, it has been described a new periodic cell composed by a central grating and two spacing layers at its sides aimed to simulate the finiteness of the device.

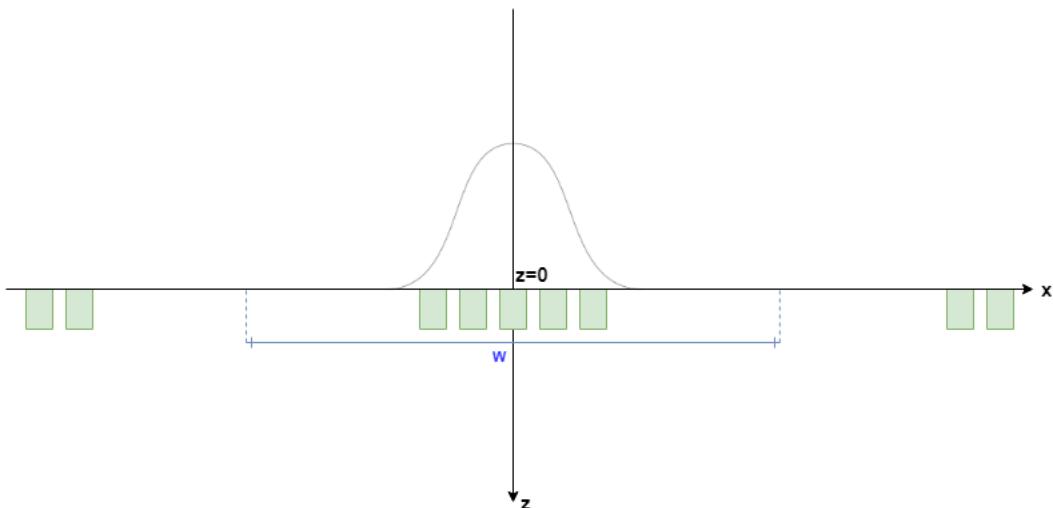


Figure 1.2: Periodic structure with Gaussian beam illuminating only one cell.

Clearly, the spacing layers are designed according to the beam waist in such a way that the incident field at the unit cell boundaries is quite negligible. In section 3.2 all simulations concerning this model have been reported.

Chapter 2

Foundations of the Rigorous Coupled-Wave Analysis applied to diffraction gratings

In this chapter, the foundations required to properly apply the *Rigorous Coupled-Wave Analysis* (RCWA) are shown, which are used to evaluate the scattering parameters of a dielectric periodic structure like a diffraction grating. RCWA is based on the modal expansions whose are used to describe both fields and dielectric structure.

In section 2.1, RCWA is formulated considering only the TE polarization and assuming in-plane incidence (i.e. $k_y = 0$) in order to study with a simpler approach the problem, without affecting the development of the method. Floquet modes are defined according to some periodic boundary conditions and their are used to represent electromagnetic fields in the homogeneous regions.

The scattering matrices related to the device are achieved in section 2.1.1 by means the so called mode-matching technique (MMT).

For sake of completeness, in section 2.2 the mode-matching technique is developed considering a generalized approach to the problem, where both TM polarization and general incidence are taken into account, as well.

2.1 Formulation of the scattering problem

A diffraction grating is an optical device characterized by multiple dielectric waveguides aimed to diffract an incident wave in several light components having different wavelengths. The grating under examination is a periodic structure expanding only in one dimension (along x , see Figure 2.1). In particular, rectangular shaped bars have been taken into account for the analysis.

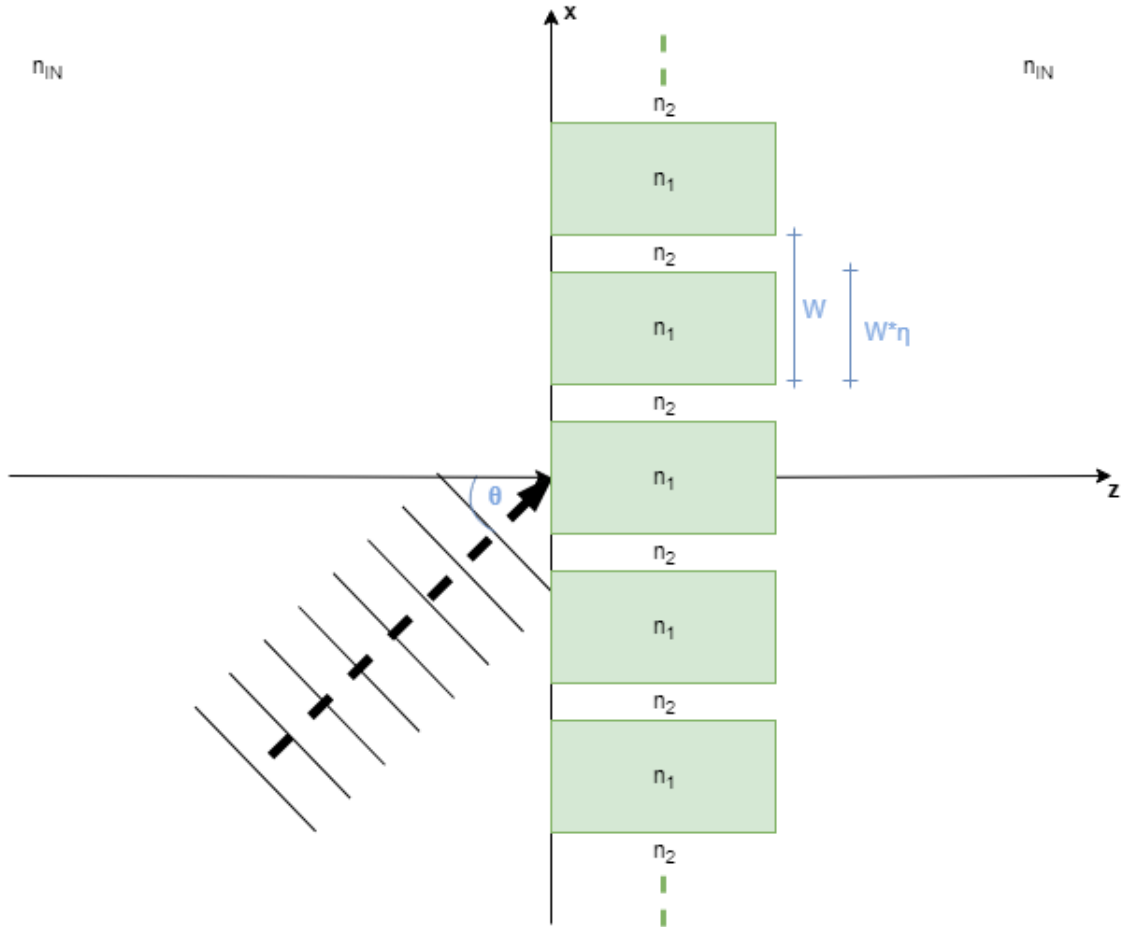


Figure 2.1: Dielectric grating with a period W , case of plane wave incident from the left. (For simplicity $n_{IN} = n_2$)

Considering the structure as replica of infinite cells, a starting point is to fix a periodic boundary condition in order to find a solution to Maxwell Equations at $z = 0$ (left half space - grating interface). To do that, Floquet modes have been employed.

$$P.B.C. : -\frac{W}{2} \leq x \leq \frac{W}{2} \quad (2.1)$$

Floquet modes yield:

$$\begin{cases} \underline{e}_m^F(x) = \frac{1}{\sqrt{W}} e^{-j\xi_m x} \hat{y} \\ \underline{h}_m^F(x) = -\frac{1}{\sqrt{W}} e^{-j\xi_m x} \hat{x} \end{cases} \quad \text{with } \xi_m = m \frac{2\pi}{W} + k_0 n_{IN} \sin \vartheta^i \quad (2.2)$$

Considering only TE-polarized fields, Maxwell Equations hold:

$$\begin{cases} -\frac{\partial E_y}{\partial z} = -j\omega\mu H_x \\ \frac{\partial E_y}{\partial x} = -j\omega\mu H_z \\ \frac{\partial H_x}{\partial z} - \frac{\partial H_z}{\partial x} = -j\omega\varepsilon(x) E_y \end{cases} \quad (2.3)$$

Using the transmission line theory, the entire fields can be expressed in terms of modal current and voltage by means the modal field expansions.

$$\begin{cases} \hat{y} E_y(x, z) = \sum_m V_m(z) \underline{e}_m^F(x) \\ \hat{x} H_x(x, z) = \sum_m I_m(z) \underline{h}_m^F(x) \\ H_z(x, z) = \frac{1}{\sqrt{W}} \sum_m H_{zm} e^{-j\xi_m x} \end{cases} \quad (2.4)$$

The next step is to project (2.3) (after properly replacing modal functions (2.4)) into $\underline{e}_p^F(x)$, with the latter orthonormal to $\underline{h}_m^F(x) \times \hat{z}$, i.e. $\langle \underline{e}_p^F(x), \underline{h}_m^F(x) \times \hat{z} \rangle = \delta_{pm}$ (more details can be found in section 2.2). Maxwell's Equations take now a new form:

$$\begin{cases} -\frac{\partial V_p}{\partial z} = -j\omega\mu I_p \\ -j\xi_p V_p = -j\omega\mu H_{zp} \\ \frac{\partial I_p}{\partial z} + j\xi_p H_{zp} = j\omega\varepsilon_0 \sum_m E_{pm} V_m \end{cases} \quad \text{with } E_{pm} = \frac{1}{W} \int n^2(x) e^{-j(\xi_m - \xi_p)x} dx \quad (2.5)$$

E_{pm} represents the Spatial Fourier Transform of $n^2(x)$, where $n(x)$ indicates the grating refractive index. However, the hypothesis of $\mu \approx \mu_0$ is assumed for the dielectrics material of this study. Obtaining H_{zp} from the second equation above, this value is replaced in the third row of (2.5) allowing to rewrite the system above with only two equations:

$$\begin{cases} -\frac{dV_p}{dz} = -j\omega\mu_0 I_p \\ \frac{dI_p}{dz} = -j \frac{\xi_p^2}{\omega\mu_0} V_p + j\omega\varepsilon_0 \sum_m E_{pm} V_m \end{cases} \quad (2.6)$$

Defining the following quantities

$$\underline{V} = \{V_p\}, \quad \underline{I} = \{I_p\}, \quad \underline{E} = E_{pm} = \frac{1}{W} \int n^2(x) e^{-j(\xi_m - \xi_p)x} dx, \quad \underline{\xi}^2 = \text{diag}\{\xi_p^2\}$$

(2.6) can be written in matrix form:

$$\begin{cases} -\frac{dV}{dz} = j\omega\mu_0 \underline{I} \\ -\frac{dI}{dz} = \frac{j}{\omega\mu_0} (k_0^2 \underline{E} - \underline{\xi}^2) V \end{cases} \quad (2.7)$$

Solving (2.7) with respect to \underline{V} , the following steps are necessary. First of all, \underline{I} has been found from the first equation:

$$\underline{I} = -\frac{1}{j\omega\mu_0} \frac{dV}{dz} \rightarrow -\frac{dI}{dz} = \frac{1}{j\omega\mu_0} \frac{d^2V}{dz^2} \quad (2.8)$$

Then, a second order ordinary differential equation (ODE) resulted replacing \underline{I} in the second row of (2.7):

$$\frac{d^2V}{dz^2} + (k_0^2 \underline{E} - \underline{\xi}^2) V = 0 \quad (2.9)$$

Assuming a solution as $\underline{V}(z) = \underline{V}_0 e^{-jk_z z}$, (2.9) has been simplified:

$$(k_0^2 \underline{E} - \underline{\xi}^2) \underline{V}_0 = k_z^2 \underline{V}_0 \quad (2.10)$$

The equation above is an eigenvalue problem, whose eigenvalues and eigenvectors are the k_z and the expansion coefficients of the "grating modes" (even called phase-shift wall waveguide PSWW modes) in the Floquet mode basis, respectively.

Considering $\underline{e}_n^P(x)$ and $\underline{h}_n^P(x) = \hat{z} \times \underline{e}_n^P$ the grating modes, they are normalized with respect to a single cell period.

$$\int_{-\frac{w}{2}}^{\frac{w}{2}} |e_n^P|^2 dx = 1 \quad (2.11)$$

The grating modes expressed above are a linear combination of Floquet ones with the eigenvectors of the eigenvalue problem of (2.10), i.e. $e_n^P = \sum_m u_{nm} e_m^F(x)$. They must be normalized in order to be orthonormal in the whole dielectric structure, therefore $\underline{e}_n^P = \frac{1}{N} \sum_m \bar{u}_{nm} e_m^F(x)$.

$$\frac{1}{N^2} \sum_m |\bar{u}_{nm}|^2 = \int |e_n^P|^2 dx = 1 \quad (2.12)$$

$$N = \sqrt{\sum_m |\bar{u}_{nm}|^2} \quad (2.13)$$

By means the condition fixed in 2.13, N value is stated and it will be used in MATLAB[®] as normalization factor.

2.1.1 Junction Problem

Considering the diffraction grating in analysis, it can be studied by means the transmission line theory, according Figure 2.2.

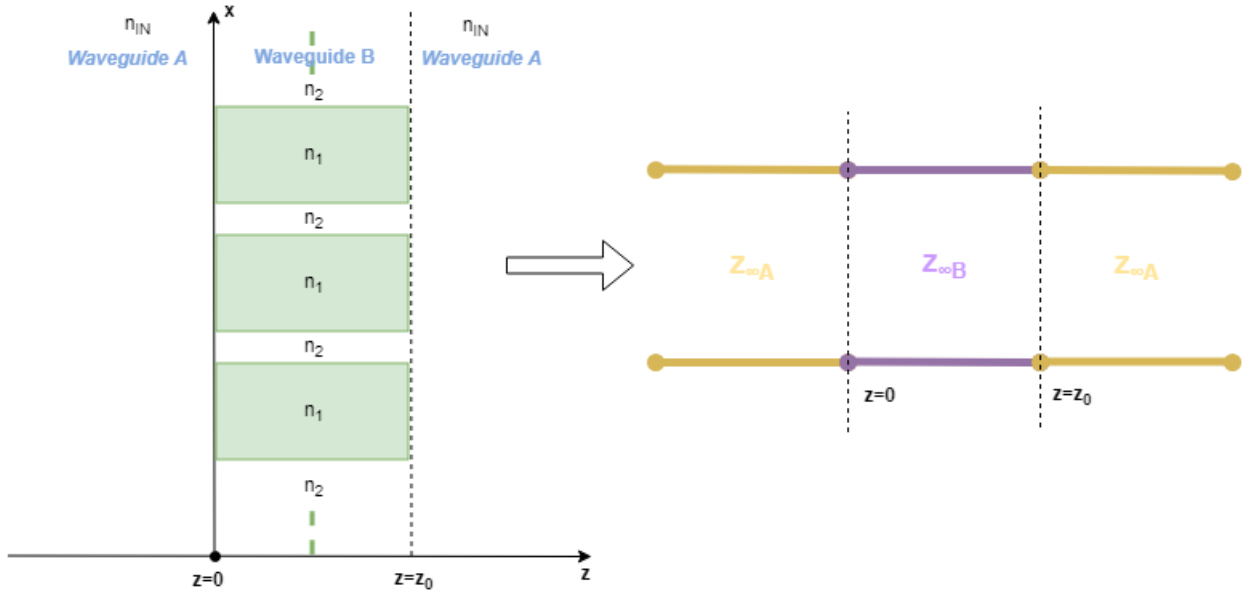


Figure 2.2: Junction problem at $z=0$.

Continuity condition is enforced on the transversal field components in correspondence of the two bars-air interfaces of Figure 2.2 in order to find the scattering parameters. Firstly, starting to imposing this condition at $z = 0$:

$$\begin{cases} E_y(x, 0^-) = E_y(x, 0^+) \\ H_x(x, 0^-) = H_x(x, 0^+) \end{cases} \quad (2.14)$$

Projecting the fields on the Floquet modes, 2.14 assumes the following form:

$$\begin{cases} \underline{e}_A(V_A^{inc} + V_A^{scat}) = \underline{e}_B(V_B^{inc} + V_B^{scat}) \\ \underline{h}_A Y_A(V_A^{inc} - V_A^{scat}) = \underline{h}_B Y_B(V_B^{inc} - V_B^{scat}) \end{cases} \quad (2.15)$$

At this point, the so called *mode matching technique* (MMT) has been performed under the conditions of TE-polarized fields and in-plane incidence ($k_y = 0$). Clearly, modes of the same waveguide must be orthonormal among themselves:

$$\begin{cases} \langle \underline{h}_B^+ \times \hat{z}, \underline{e}_B \rangle = \delta \\ \langle \hat{z} \times \underline{e}_A^+, \underline{h}_A \rangle = \delta \end{cases} \quad (2.16)$$

Then, projection matrices T and T^+ have been defined below as the scalar product among modes of different waveguides.

$$\begin{cases} \langle \underline{h}_B^+ \times \hat{z}, \underline{e}_A \rangle = T = \int \underline{h}_B^* \times \hat{z} \cdot \underline{e}_A dx \\ \langle \hat{z} \times \underline{e}_A^+, \underline{h}_B \rangle = T^+ = \int \underline{h}_B \times \hat{z} \cdot \underline{e}_A^* dx \end{cases} \quad (2.17)$$

Referring to the transmission line model of Figure 2.2, the interface at $z = 0$ has been analysed and equations representing the equivalent voltages have been written below.

$$\begin{cases} T(V_A^{inc} + V_A^{scat}) = V_B^{inc} + V_B^{scat} \\ Y_A(V_A^{inc} - V_A^{scat}) = T^+ Y_B (V_B^{scat} - V_B^{inc}) \end{cases} \quad (2.18)$$

Now, the superposition principle has been exploited to solve the system above. Assuming $V_B^{inc} = 0$, (2.18) simplifies:

$$\begin{cases} T(V_a^{inc} + V_a^{scat}) = V_B^{scat} \\ Y_A(V_A^{inc} - V_A^{scat}) = T^+ Y_B V_B^{scat} \end{cases} \rightarrow \begin{cases} V_B^{scat} = T(V_a^{inc} + V_a^{scat}) \\ Y_A(V_A^{inc} - V_A^{scat}) = T^+ Y_B T(V_A^{inc} + V_A^{scat}) \end{cases} \quad (2.19)$$

Collecting V_A^{scat} in the second equation of (2.19), it can be exposed in a simpler form.

$$Q V_A^{scat} = (Y_A - T^+ Y_B T) V_A^{inc}, \quad \text{with } Q = T^+ Y_B T + Y_A \quad (2.20)$$

Concluding, equivalent voltages of the transmission line model related to the condition $V_B^{inc} = 0$ have been calculated, replacing (2.20) in (2.19).

$$\begin{cases} V_B^{scat} = T[1 + Q^{-1}(Y_A - T^+ Y_B T)] V_A^{inc} \\ V_A^{scat} = Q^{-1}(Y_A - T^+ Y_B T) V_A^{inc} \end{cases} \quad (2.21)$$

The condition $V_A^{inc} = 0$ has been fixed now in order to find the last contributions of scattered voltages in this junction. The way of proceeding is identical of that performed in (2.19).

$$\begin{cases} V_B^{scat} = TV_A^{scat} - V_B^{inc} \\ -Y_A V_A^{scat} = T^+ Y_B (V_B^{scat} - V_B^{inc}) \end{cases} \quad (2.22)$$

V_B^{scat} obtained in the first equation is used in the second one in order to express V_A^{scat} :

$$\begin{aligned} -Y_A V_A^{scat} &= T^+ Y_B (TV_A^{scat} - 2V_B^{inc}) \\ (Y_A - T^+ Y_B T) V_A^{scat} &= 2T^+ Y_B V_B^{inc} \end{aligned}$$

The system (2.22) is solved with respect to the scattered voltages and the equations are expressed in (2.23), with the value of Q shown in (2.20).

$$\begin{cases} V_B^{scat} = (2TQ^{-1}T^+ Y_B - 1)V_B^{inc} \\ V_A^{scat} = 2Q^{-1}T^+ Y_B V_B^{inc} \end{cases} \quad (2.23)$$

Scattering parameters can be represented by using the concept of wave amplitudes. In general, this physical quantity is expressed as $a = \sqrt{Y_i} V_i^{inc}$ if it is referred to an incident wave or $b = \sqrt{Y_i} V_i^{scat}$ in the scattering case. The scheme drawn in 2.3 could be useful for understanding this concept.

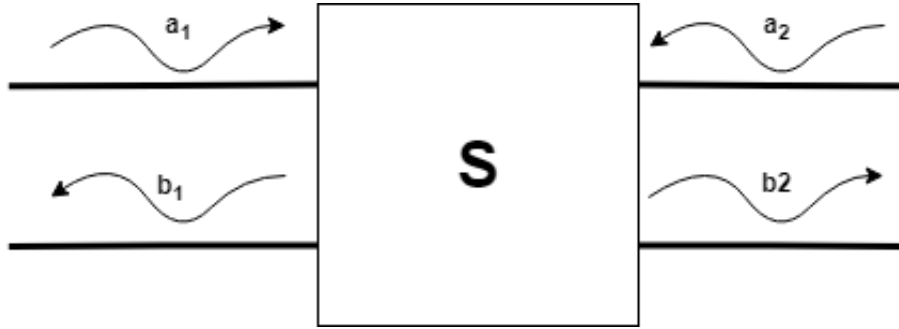


Figure 2.3: Scattering block representing an interface.

Scattering parameters are defined according to the following linear system:

$$\begin{cases} b_1 = a_1 S_{11} + a_2 S_{12} \\ b_2 = a_1 S_{21} + a_2 S_{22} \end{cases} \quad (2.24)$$

Expressing a_i and b_i in terms of modal voltages, the first row of (2.24) has been solved by considering the second rows of both (2.21) and (2.23), since $b_1 = \sqrt{Y_A} V_A^{scat}$. On

the contrary, S_{21} and S_{22} have been found at the same manner by means the remained equations of the aforementioned systems.

$$\begin{cases} S_{11} = \frac{b_1}{a_1} |_{a_2=0} = \frac{V_A^{scat} \sqrt{Y_A}}{V_B^{inc} \sqrt{Y_A}} |_{V_B^{inc}=0} = \sqrt{Y_A} Q^{-1} (Y_A - T^+ Y_B T) \sqrt{Z_A} \\ S_{12} = \frac{b_1}{a_2} |_{a_1=0} = \frac{V_A^{scat} \sqrt{Y_A}}{V_B^{inc} \sqrt{Y_B}} |_{V_A^{inc}=0} = 2\sqrt{Y_A} Q^{-1} T^+ Y_B \sqrt{Z_B} \\ S_{21} = \frac{b_2}{a_1} |_{a_2=0} = \frac{V_B^{scat} \sqrt{Y_B}}{V_A^{inc} \sqrt{Y_A}} |_{V_B^{inc}=0} = \sqrt{Y_B} T [1 + Q^{-1} (Y_A - T^+ Y_B T)] \sqrt{Z_A} \\ S_{22} = \frac{b_2}{a_2} |_{a_1=0} = \frac{V_B^{scat} \sqrt{Y_B}}{V_A^{inc} \sqrt{Y_B}} |_{V_A^{inc}=0} = \sqrt{Y_B} (2T Q^{-1} T^+ Y_B - 1) \sqrt{Z_B} \end{cases} \quad (2.25)$$

In order to evaluate the complete scattering matrix of the system, now the scattering parameters related to the junction at $z = z_0$ must be evaluated. The first step is, like in the previous case, to enforce the *continuity condition* of the field transversal components at the aforementioned bars-air interface.

$$\begin{cases} E_y(x, z_0^-) = E_y(x, z_0^+) \\ H_x(x, z_0^-) = H_x(x, z_0^+) \end{cases} \quad (2.26)$$

Performing projection on Floquet modes, (2.26) can be rewritten exactly as done in (2.15). Clearly, what changes now with respect to the previous case is the disposition of the two waveguides, with the one associated to the grating on the left of the junction and the other one related to the half space is placed on the right. Applying the MMT, achieved equations are quite similar of that one in (2.18).

$$\begin{cases} V_B^{inc} + V_B^{scat} = T(V_A^{inc} + V_A^{scat}) \\ T^+ Y_B (V_B^{inc} - V_B^{scat}) = Y_A (V_A^{scat} - V_A^{inc}) \end{cases} \quad (2.27)$$

The way to proceed is identical to (2.19), indeed superposition principle has been exploited again. Firstly, considering $V_A^{inc} = 0$, (2.27) holds:

$$\begin{cases} V_B^{scat} = T V_A^{scat} - V_B^{inc} \\ T^+ Y_B (2V_B^{inc} - T V_A^{scat}) = Y_A V_A^{scat} \end{cases} \rightarrow \begin{cases} V_B^{scat} = T V_A^{scat} - V_B^{inc} \\ 2T^+ Y_B V_B^{inc} - T^+ Y_B T V_A^{scat} = Y_A V_A^{scat} \end{cases} \quad (2.28)$$

From the second equation of (2.28) the V_A^{scat} must be evaluated, therefore this term is grouped in the first term:

$$(T^+ Y_B T + Y_A) V_A^{scat} = Q V_A^{scat} = 2T^+ Y_B V_B^{inc}$$

Substituting the V_A^{scat} value in the first equation of (2.28), the final result yields:

$$\begin{cases} V_B^{scat} = (2TQ^{-1}T^+Y_B - 1)V_B^{inc} \\ V_A^{scat} = 2Q^{-1}T^+Y_BV_B^{inc} \end{cases} \quad (2.29)$$

Now the hypothesis of $V_B^{inc} = 0$ has been applied in (2.27) in order to obtain the remained contributions used to find both S_{12} and S_{22} , respectively.

$$\begin{cases} V_B^{scat} = T(V_A^{inc} + V_A^{scat}) \\ -T^+Y_BV_B^{scat} = Y_A(V_A^{scat} - V_A^{inc}) \end{cases} \rightarrow \begin{cases} V_B^{scat} = T(V_A^{inc} + V_A^{scat}) \\ -T^+Y_BT(V_A^{inc} + V_A^{scat}) = Y_A(V_A^{scat} - V_A^{inc}) \end{cases} \quad (2.30)$$

The method is identical to the previous one, with the scattering parameters evaluated according to the incident voltage V_A^{inc} . The second equation has been developed aiming to express V_A^{scat} :

$$\begin{aligned} -T^+Y_BTV_A^{inc} - T^+Y_BTV_A^{scat} &= Y_AV_A^{scat} - Y_AV_A^{inc} \\ (T^+Y_BT + Y_A)V_A^{scat} &= (Y_A - T^+Y_BT)V_A^{inc} \\ QV_A^{scat} &= (Y_A - T^+Y_BT)V_A^{inc} \end{aligned}$$

Replacing V_A^{scat} in the first equation of the system (2.30), the last scattered term related to the condition $V_B^{inc} = 0$ has been obtained.

$$\begin{cases} V_B^{scat} = T[1 + Q^{-1}(Y_A - T^+Y_BT)]V_A^{inc} \\ V_A^{scat} = Q^{-1}(Y_A - T^+Y_BT)V_A^{inc} \end{cases} \quad (2.31)$$

The scattering matrix construction referred to the junction at $z = z_0$ has been made using the same principles already expressed in (2.24), considering the grating B on the left and the homogeneous space A on the right.

$$\begin{cases} S_{11} = \frac{b_1}{a_1}|_{a_2=0} = \frac{V_B^{scat}\sqrt{Y_B}}{V_B^{inc}\sqrt{Y_B}}|_{V_A^{inc}=0} = \sqrt{Y_B}(2TQ^{-1}T^+Y_B - 1)\sqrt{Z_B} \\ S_{12} = \frac{b_1}{a_2}|_{a_1=0} = \frac{V_B^{scat}\sqrt{Y_B}}{V_A^{inc}\sqrt{Y_A}}|_{V_B^{inc}=0} = \sqrt{Y_B}T[1 + Q^{-1}(Y_A - T^+Y_BT)]\sqrt{Z_A} \\ S_{21} = \frac{b_2}{a_1}|_{a_2=0} = \frac{V_A^{scat}\sqrt{Y_A}}{V_B^{inc}\sqrt{Y_B}}|_{V_A^{inc}=0} = 2\sqrt{Y_A}Q^{-1}T^+Y_B\sqrt{Z_B} \\ S_{22} = \frac{b_2}{a_2}|_{a_1=0} = \frac{V_A^{scat}\sqrt{Y_A}}{V_B^{inc}\sqrt{Y_A}}|_{V_B^{inc}=0} = \sqrt{Y_A}Q^{-1}(Y_A - T^+Y_BT)\sqrt{Z_A} \end{cases} \quad (2.32)$$

As expected, the scattering parameters of the junction at $z = z_0$ are symmetric to that ones at $z = 0$, since the formers refer to the same system of the latter but with different orientation (at $z = 0$ grating is on the right, homogeneous space on the left).

The last step consisted perform the cascade among these two scattering matrices, as conceptually shown in Figure 2.4.

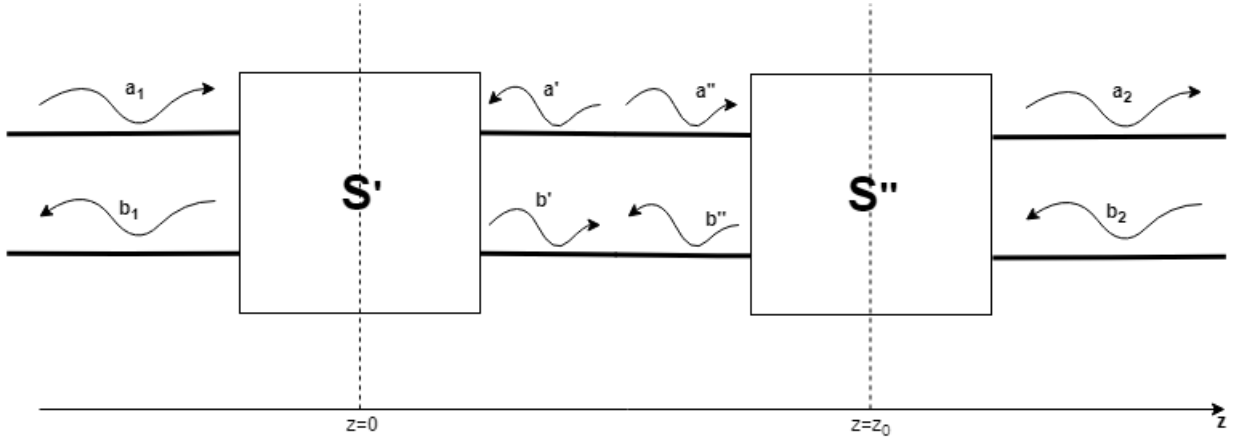


Figure 2.4: The two junctions represented by two scattering matrices in cascade configuration.

The connection of two devices like in this case is possible, assuming that the number of output ports N of \mathbf{S}' is equal to the number of input ports of \mathbf{S}'' . Furthermore, supposing that the ports whose must be connected have the same input impedance, the following equation holds:

$$\begin{cases} a' = b'' \\ a'' = b' \end{cases} \quad (2.33)$$

Only mathematical calculation are made at this point [7], therefore the scattering parameters of the device have been completely reported just below.

$$\begin{cases} S_{11} = S'_{11} + S'_{12}S''_{11}(1 - S'_{22}S''_{11})^{-1}S'_{21} \\ S_{12} = S'_{12}(1 - S'_{22}S''_{11})^{-1}S''_{12} \\ S_{21} = S''_{21}(1 - S'_{22}S''_{11})^{-1}S'_{21} \\ S_{22} = S''_{22} + S''_{21}(1 - S'_{22}S''_{11})^{-1}S'_{22}S''_{12} \end{cases} \quad (2.34)$$

The fields reconstruction has been made by means the modal voltages (and currents). Fixing $a_2 = 0$ from the system of Figure 2.4 and setting $R = \frac{1}{1 - S'_{22}S''_{11}}$, power waves in the loop can be expressed in the following manner:

$$\begin{cases} b' = RS'_{21}a_1 \\ a' = S''_{11}b' \\ a'' = e^{-j\beta_0 z}b' \\ b'' = S''_{11}a'' \end{cases} \quad (2.35)$$

Considering also $b_1 = S_{11}a_1$, the equivalent voltages yields:

$$\left\{ \begin{array}{l}
 V(z = 0^-) = \sqrt{Z_F}(a_1 + b_1) \\
 I(z = 0^-) = \sqrt{Y_F}(a_1 - b_1) \\
 \\
 V(z = 0^+) = \sqrt{Z_G}(a' + b') \\
 I(z = 0^+) = \sqrt{Y_G}(a' - b') \\
 \\
 V(z = z_0^-) = \sqrt{Z_G}(a'' + b'') \\
 I(z = z_0^-) = \sqrt{Y_G}(a'' - b'') \\
 \\
 V(z = z_0^+) = \sqrt{Z_F}b_2 \\
 I(z = z_0^+) = \sqrt{Y_F}b_2
 \end{array} \right. \quad (2.36)$$

In general, values obtained in (2.36) give an indication of the spatial Fourier transform both of the y-component of electric field (E_y) by means the voltages, and the x-component of magnetic field (H_x) using the current.

Numerically speaking, it is possible to build a matrix called $FLOQMAT = e^{-jx\xi_p}$ (see Section 2.1 for ξ_p) aimed to perform the inverse spatial Fourier transform. Moreover, in order to execute correctly the mode matching, normalized modes (achieved in (2.12)) and hence normalized eigenvector of the A matrix ($A = k_0^2 \underline{E} - \underline{\xi}$, according to (2.10)) must be used for the fields outside the grating. Eigenvectors are arranged in Mv , a matrix having a number of columns equal to the number of modes under analysis, while rows agree the ξ_p resolution of the selected Floquet modes.

$$\left\{ \begin{array}{l}
 E_y(z = 0^-) = FLOQMAT \times Mv \times V(z = 0^-) \\
 H_x(z = 0^-) = FLOQMAT \times Mv \times I(z = 0^-) \\
 \\
 E_y(z = 0^+) = \frac{1}{\sqrt{W}} \times FLOQMAT \times V(z = 0^+) \\
 H_x(z = 0^+) = \frac{1}{\sqrt{W}} \times FLOQMAT \times I(z = 0^+) \\
 \\
 E_y(z = z_0^-) = \frac{1}{\sqrt{W}} \times FLOQMAT \times V(z = z_0^-) \\
 H_x(z = z_0^-) = \frac{1}{\sqrt{W}} \times FLOQMAT \times I(z = z_0^-) \\
 \\
 E_y(z = z_0^+) = FLOQMAT \times Mv \times V(z = z_0^+) \\
 H_x(z = z_0^+) = FLOQMAT \times Mv \times I(z = z_0^+)
 \end{array} \right. \quad (2.37)$$

For what concerns fields inside the grating in (2.37), normalization condition of the mode has to be complied using the normalization factor $\frac{1}{\sqrt{W}}$, according to (2.11) with W the stated cell period of the dielectric profile.

2.1.2 Reconstruction of the dielectric profile

Unit cell with single bar

As shown at the beginning of section 2.1, it is useful to find the square value of the profile index $n^2(x)$ in such a way to check the matrix $E_{pm} = \underline{E}$ of (2.5). By the way, description of the refractive index referred to a unit cell is done passing from some analytical calculation. Starting to consider a grating period like that one of Figure 2.5:

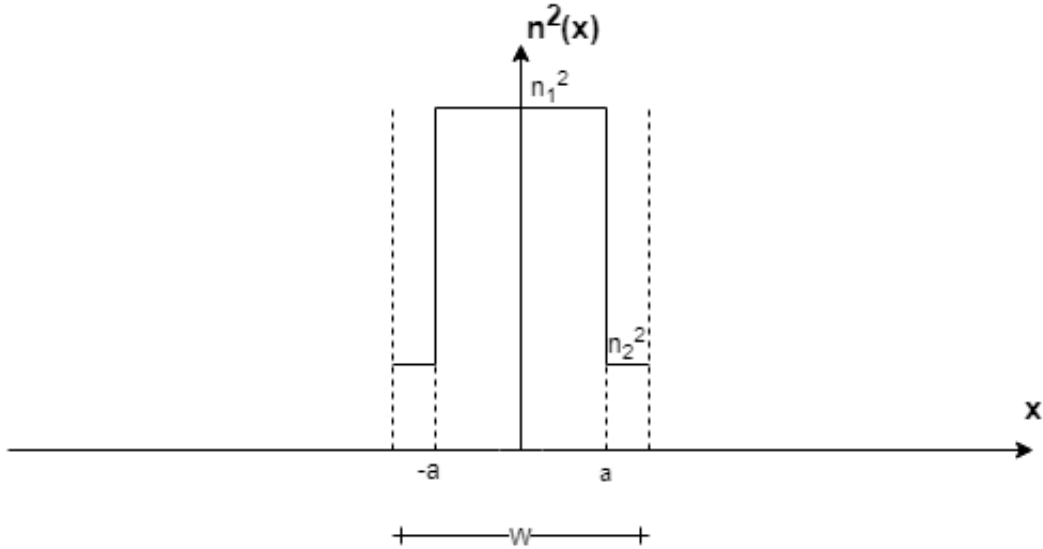


Figure 2.5: Dielectric profile of a single bar having a refractive index n_1 .

This dielectric profile is representable in the spectral domain using Spatial Fourier Transform (SFT). In following, Figure 2.5 is described in an analytical form:

$$n^2(x) = n_2^2 + (n_1^2 - n_2^2)rect(x, 2a) \quad (2.38)$$

Applying the spatial Fourier transform to (2.38) $\rightarrow N^2(\xi_p) = \mathcal{F}\{n^2(x)\} = \int n^2(x)e^{j\xi_p x} dx$:

$$N^2(\xi_p) = n_2^2 \frac{1}{W} \int_{-\frac{W}{2}}^{\frac{W}{2}} e^{j\xi_p x} dx + (n_1^2 - n_2^2) \frac{2a}{W} \frac{\sin \frac{2a\xi_p}{2}}{\frac{2a\xi_p}{2}}$$

$$N^2(\xi_p) = n_2^2 \delta_{p0} + (n_1^2 - n_2^2) \frac{2a}{W} \frac{\sin(a\xi_p)}{(a\xi_p)} \quad (2.39)$$

The correctness of E_{pm} matrix can be validated in the simulation by reconstructing the cell dielectric profile using Floquet modes, comparing results with the exact value of $n^2(x)$, as shown in Figure 3.3 of the Chapter 3.

Unit cell with multiple bars

Considering now a more complex case than before, with three bars in a single cell period W greater 3 times the previous case. Although the cell structure is different with respect Figure 2.5, maintaining the same bar-filler proportion ($b = W_{PreviousCase} - 2a$), the grating in analysis is remained exactly the same of before. Therefore, in this subsection the new value of $N^2(\xi_p)$ has to be evaluated in order to verify (in the next chapter), by means MATLAB®[®], that the scattering behaviour of the dielectric structure remained unchanged with respect to the previous case having an unit cell like in Figure 2.5. Calculations are quite similar to (2.39), with bars replicated and translated along the x direction.

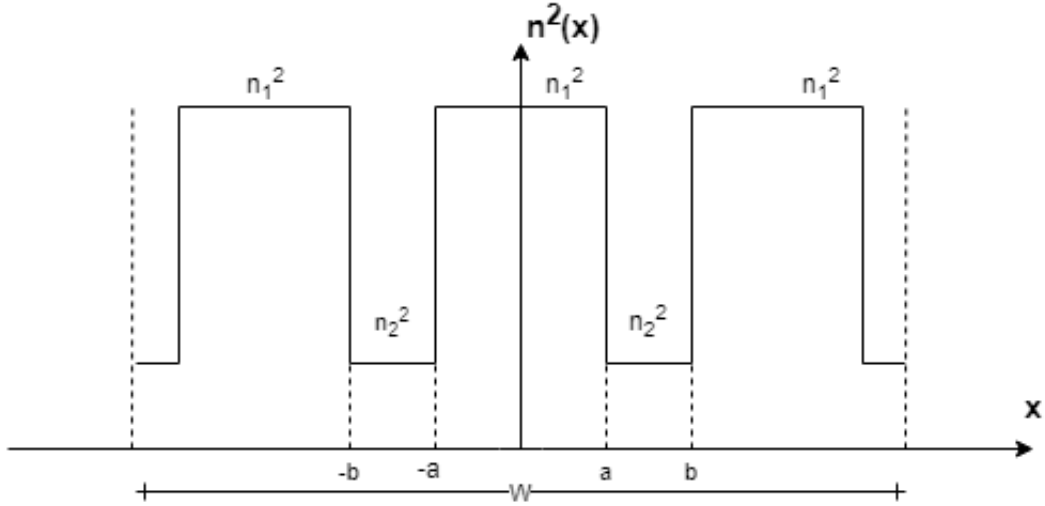


Figure 2.6: Unit cell of grating profile composed by 3 bars and a duty-cycle of 67%.

The presence of two bars translated by $\pm(a+b)$ quantity are now present in a single elementary cell, hence the analytical description of the profile in Figure 2.6 is:

$$n^2(x) = n_2^2 + (n_1^2 - n_2^2) \{ \text{rect}(x, 2a) + \text{rect}[x - (a+b), 2a] + \text{rect}[x + (a+b), 2a] \} \quad (2.40)$$

Applying SFT to (2.40), translations are exponentials with imaginary argument:

$$N^2(\xi_p) = n_2^2 \delta(\xi_p) + (n_1^2 - n_2^2) \left\{ \frac{2a \sin(\frac{2a\xi_p}{2})}{W \frac{2a\xi_p}{2}} + \frac{2a \sin(\frac{2a\xi_p}{2})}{W \frac{2a\xi_p}{2}} [e^{-j(a+b)\xi_p} + e^{j(a+b)\xi_p}] \right\} \quad (2.41)$$

In (2.41) exponentials can be grouped in terms of a cosine:

$$N^2(\xi_p) = n_2^2 \delta(\xi_p) + (n_1^2 - n_2^2) \frac{2a \sin(a\xi_p)}{W a\xi_p} \{ 1 + 2 \cos[\xi_p(a+b)] \} \quad (2.42)$$

Case of Figure 2.6 can be generalized for a greater odd number of bars per unit cell and this fact is used in Chapter 3 in order to reconstruct a periodic cell behaving almost as a "grating of finite extent".

$$N^2(\xi_p) = n_2^2 \delta(\xi_p) + (n_1^2 - n_2^2) \frac{2a}{W} \frac{\sin(a\xi_p)}{a\xi_p} \left\{ 1 + 2 \sum_{m=1}^{\frac{n_{bars}-1}{2}} \cos[m\xi_p(a+b)] \right\} \quad (2.43)$$

Case of extents at the cell boundaries

In the thesis's introductory chapter, it has been explained how the construction of a periodic profile, composed by a finite number of elementary cells replicated with a very long period, could behave like a grating with finite extent. In order to analytically realize such structure, it is possible to extend the filler dielectric material at the grating boundaries for a very long length.

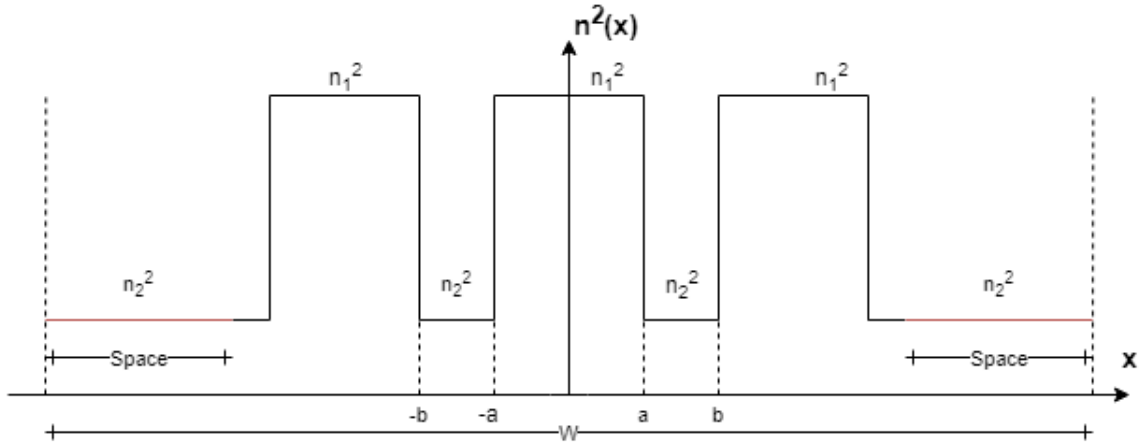


Figure 2.7: Unit cell with periodic bars and extents.

The analytical description of the model does not differ from the previous one, since the presence of the "spacing layers" at the grating sides is arithmetically justified with the extension of period W . Greater unit cell involves to get also a smaller ξ according to (2.2), therefore in the Chapter 3 is shown how the reconstructed index profile changes accordingly.

From the exact to a good approximated dielectric profile

In section 2.1.2, bars have been seen as perfect squared entities with refractive index n_1 . In the real case, raised-cosine shape is a better approximation to describe real refractive index profile of the bars.

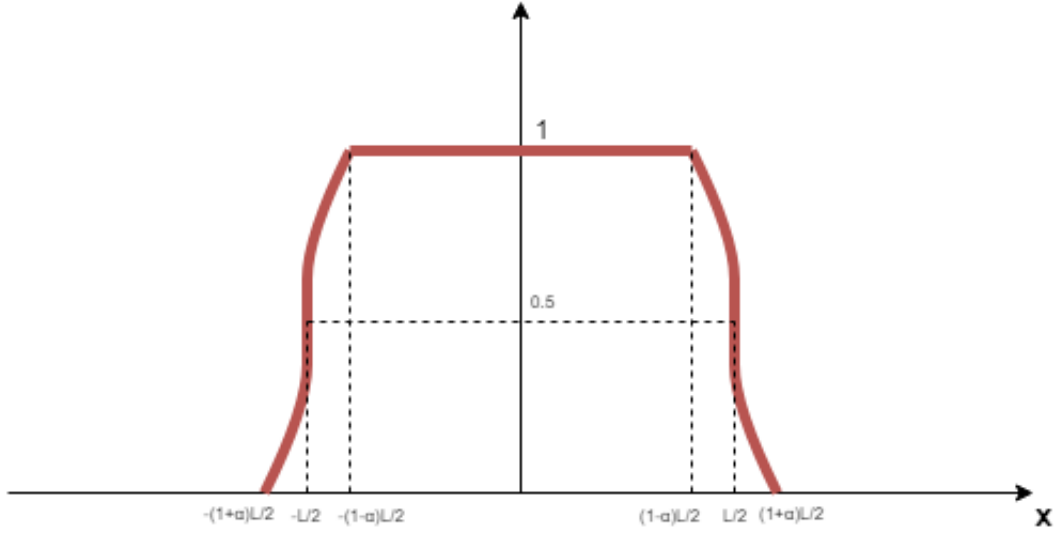


Figure 2.8: Example of a raised-cosine function

Where α represents the so called "roll-off" factor. When the latter is null, Figure 2.8 is a simple rect signal. On the contrary, if $\alpha = 1$ the raised-cosine function degenerate into a kind of Gaussian bell. In mathematical form, this kind of curve can be resumed as shown in (2.44).

$$RC(x) = \begin{cases} 1 & \text{if } |x| < \frac{(1-\alpha)L}{2} \\ \frac{1}{2} \{1 - \sin[\frac{\pi}{\alpha}(\frac{|x|}{L} - \frac{1}{2})]\} & \end{cases} \quad (2.44)$$

Without reporting any calculation, the SFT of a raised cosine has been written in (2.45). It is interesting to see how the only difference with the spatial transform of the rect used previously to describe the bar refractive index is the red coloured part, therefore the value of $N^2(\xi_p)$ already evaluated before is still valid in this case by considering the red term as well.

$$\mathcal{F}\{RC(x)\} = L \frac{\sin(\frac{\xi L}{2})}{\frac{\xi L}{2}} \frac{\cos(\frac{\alpha \xi L}{2})}{1 - (\frac{2\alpha \xi L}{\pi})^2} \quad (2.45)$$

The discontinuity in (2.45) at $\frac{\alpha \xi L}{2} \rightarrow \frac{\pi}{2}$ is solved as follow, renaming $\frac{\alpha \xi L}{2} = x$ only in (2.46) for simplicity.

$$\lim_{x \rightarrow \frac{\pi}{2}} \frac{\cos(x)}{1 - (\frac{2x}{\pi})^2} = \frac{\pi}{4} \quad (2.46)$$

2.2 MMT - Focus on Projection matrices

In section 2.1.1 the junction problem has already been faced considering the projection matrices T and T^+ as a result of the scalar product among modes, as seen in (2.63). Although in Chapter 3 the studies are focused considering only TE polarization and in-plane incidence ($k_y = 0$), a general analysis of the projection matrices is surely useful to better understand the method of mode-matching technique. Starting from the continuity condition of (2.15), that system is rewritten using the modal field expansion.

$$\begin{cases} \sum_p (V_{A,p}^{inc} + V_{A,p}^{scat}) \underline{e}_{A,p}(x, y) = \sum_m (V_{B,m}^{inc} + V_{B,m}^{scat}) \underline{e}_{B,m}(x, y) \\ \sum_p Y_{A,p} (V_{A,p}^{inc} - V_{A,p}^{scat}) \underline{h}_{A,p}(x, y) = \sum_m Y_{B,m} (V_{B,m}^{inc} + V_{B,m}^{scat}) \underline{h}_{B,m}(x, y) \end{cases} \quad (2.47)$$

(2.47) refers to the junctions present in the model of Figure 2.2, where the system has been resumed as three different wave guides (two related to the homogeneous media A and one associated to the grating B) along z . Performing the modal projection at the junctions (at $z = 0$ and $z = z_0$, respectively), the so called *Weak Formulation* of the problem has been built in (2.48).

$$\begin{cases} \sum_p (V_{A,p}^{inc} + V_{A,p}^{scat}) \langle \underline{h}_{B,n}^+ \times \hat{z}, \underline{e}_{A,p} \rangle = \sum_m \langle \underline{h}_{B,n}^+ \times \hat{z}, \underline{e}_{B,m} \rangle (V_{B,m}^{inc} + V_{B,m}^{scat}) \\ \sum_p Y_{A,p} (V_{A,p}^{inc} - V_{A,p}^{scat}) \langle \hat{z} \times \underline{e}_{A,n}^+, \underline{h}_{A,p} \rangle = \sum_m Y_{B,m} \langle \hat{z} \times \underline{e}_{A,n}^+, \underline{h}_{B,m} \rangle (V_{B,m}^{inc} - V_{B,m}^{scat}) \end{cases} \quad (2.48)$$

From the formulation above, the two projection matrices related to iteration among the waveguides are fixed. In particular, in the case of a grating between two homogeneous media, the latter are marked with a F subscript, instead the former is indicated with the G letter.

$$\begin{cases} (\underline{T}_{GF}^{(e)})_{mp} = \langle \underline{h}_{Gm}^+ \times \hat{z}, \underline{e}_{F,p} \rangle \\ (\underline{T}_{FG}^{(h)})_{pm} = \langle \hat{z} \times \underline{e}_{F,p}^+, \underline{h}_{G,m} \rangle \end{cases} \quad (2.49)$$

Clearly, the projection matrices just above correspond to that ones achieved in section 2.1.1, i.e. $\underline{T}_{GF}^{(e)} = T$ and $\underline{T}_{FG}^{(h)} = T^+$, respectively. First of all, the expression of Floquet modes related to the half spaces[5] are exposed below:

$$\begin{cases} \underline{e}'_p = \frac{j}{\sqrt{d}} \left[\frac{k_{xp}}{k_{tp}} \hat{x} + \frac{k_y}{k_{tp}} \hat{y} \right] e^{-jk_{xp}x} \\ \underline{h}'_p = \hat{z} \times \underline{e}'_p = \frac{j}{\sqrt{d}} \left[\frac{k_{xp}}{k_{tp}} \hat{y} - \frac{k_y}{k_{tp}} \hat{x} \right] e^{-jk_{xp}x} \\ \underline{h}''_p = \frac{j}{\sqrt{d}} \left[\frac{k_{xp}}{k_{tp}} \hat{x} + \frac{k_y}{k_{tp}} \hat{y} \right] e^{-jk_{xp}x} \\ \underline{e}''_p = \underline{h}''_p \times \hat{z} = \frac{j}{\sqrt{d}} \left[-\frac{k_{xp}}{k_{tp}} \hat{y} + \frac{k_y}{k_{tp}} \hat{x} \right] e^{-jk_{xp}x} \end{cases} \quad (2.50)$$

For what concerns the so called phase-shift wall waveguide (PSWW) devices[6], other proper modes have been used for the grating structure and they are expressed in (2.51).

$$\begin{cases} \underline{e}'_m = \left[\frac{I'_m(x)}{n^2(x)} \hat{x} - \frac{V'_m(x)}{Z'_{Gm}} \frac{k_y}{k_{zm}} \right] \\ \underline{h}'_m = I'_n(x) \hat{y} \\ \underline{e}''_m = V''_m(x) \hat{y} \\ \underline{h}''_m = \left[-V''_m(x) \hat{x} + Z_{Gm} I''_m \frac{k_y}{k''_{zm}} \hat{y} \right] \end{cases} \quad (2.51)$$

Now, it is possible to analyse a first interface having the grating on the left and homogeneous space on the right. According to that, modes have been handled in (2.52) in order to perform projections.

$$\begin{cases} \underline{h}^{'+}_{Gm} \times \hat{z} = I_n^{'+}(x) \hat{x} \\ \underline{h}^{''+}_{Gm} \times \hat{z} = \left[V_m^{''+}(x) \hat{y} + Z''_{Gm} I_m^{''+}(x) \frac{-k_y}{k''_{zm}} \hat{x} \right] \\ \underline{e}'_{Fp} = \frac{j}{k_{tp}} \left[k_{xp} \hat{x} + k_y \hat{y} \right] \frac{e^{-jk_{xp}x}}{\sqrt{d}} \\ \underline{e}''_{Fp} = \frac{j}{k_{tp}} \left[-k_{xp} \hat{y} + k_y \hat{x} \right] \frac{e^{-jk_{xp}x}}{\sqrt{d}} \end{cases} \quad (2.52)$$

Besides to consider the k_y contribution, even TM polarization have been taken into account in this section. The latter assumption brings the projection matrix to be much greater than that one used in section 2.1.1 (highlighted in red in (2.53)). Starting with the analysis of the aforementioned interface (i.e. that one at $z = z_0$, referring to Figure 2.2), complete projection matrix has been written just below.

$$\underline{\underline{T}}_{GF}^{(e)} = \begin{bmatrix} \underline{\underline{T}}_{GTEFTE}^{(e)} & \underline{\underline{T}}_{GTEFTM}^{(e)} \\ \underline{\underline{T}}_{GTMFTE}^{(e)} & \underline{\underline{T}}_{GTMFTM}^{(e)} \end{bmatrix} \quad (2.53)$$

Developing (2.49) with (2.52) both for TE and TM cases, the projection matrices have been completely obtained, remembering again that k_y is no longer null. Starting with the evaluation of $\underline{\underline{T}}_{GF}^{(e)}$:

$$\begin{aligned} (\underline{\underline{T}}_{GTEFTE})_{mp}^{(e)} &= \int_0^d \left[Z''_{Gm} I_m^{''+}(x) \frac{-k_y}{k''_{zm}} \hat{x} + V_m^{''+}(x) \hat{y} \right] \cdot \frac{j}{k_{tp}} \left[-k_{xp} \hat{y} + k_y \hat{x} \right] \frac{e^{-jk_{xp}x}}{\sqrt{d}} dx = \\ &= -j \frac{Z''_{Gm} k_y^2}{k''_{zm} k_{tp}} \frac{1}{d} \int_0^d \sum_n I_{mn}^{''+} e^{-j(k_{xp} - \xi_n)x} dx - j \frac{k_{xp}}{k_{tp}} \frac{1}{d} \int_0^d \sum_n V_{mn}^{''+} e^{-j(k_{xp} - \xi_n)x} dx = \\ &= -j \frac{Z''_{Gm} k_y^2}{k''_{zm} k_{tp}} (\underline{\underline{I}}^{''+})_{mp} - j \frac{k_{xp}}{k_{tp}} (\underline{\underline{V}}^{''+})_{mp} = -jk_y^2 \text{diag} \left\{ \frac{Z''_{Gm}}{k''_{zm}} \right\} \underline{\underline{I}}^{''+} \text{diag} \left\{ \frac{1}{k_{tp}} \right\} - j \underline{\underline{V}}^{''+} \text{diag} \left\{ \frac{k_{xp}}{k_{tp}} \right\} \end{aligned} \quad (2.54)$$

$$\begin{aligned}
 (\underline{T}_{\underline{GTEFTM}}^{(e)})_{mp} &= \int_0^d [Z''_{Gm} I''_m(x) \frac{-k_y}{k''_{zm}} \hat{x} + V''_m(x) \hat{y}] \cdot \frac{j}{k_{tp}} [k_{xp} \hat{y} + k_y \hat{x}] \frac{e^{-jk_{xp}x}}{\sqrt{d}} dx = \\
 &= -j \frac{k_{xp} k_y Z''_{Gm}}{k_{tp} k''_{zm}} \int_0^d I''_m(x) \frac{e^{-jk_{xp}x}}{\sqrt{d}} dx + j \frac{k_y}{k_{tp}} \int_0^d V''_m(x) \frac{e^{-jk_{xp}x}}{\sqrt{d}} dx = \\
 &= -j \frac{k_{xp} k_y Z''_{Gm}}{k_{tp} k''_{zm}} \sum_n I''_{mn} \frac{1}{d} \int_0^d e^{-j(k_{xp} - \xi_n)x} dx + j \frac{k_y}{k_{tp}} \sum_n V''_{mn} \frac{1}{d} \int_0^d e^{-j(k_{xp} - \xi_n)x} dx = \\
 &\quad - j k_y \text{diag}\left\{ \frac{Z''_{Gm}}{k''_{zm}} \right\} \underline{I}''_+ \text{diag}\left\{ \frac{k_{xp}}{k_{tp}} \right\} + j k_y \underline{V}''_+ \text{diag}\left\{ \frac{1}{k_{tp}} \right\} \quad (2.55)
 \end{aligned}$$

$$\begin{aligned}
 (\underline{T}_{\underline{GTMFTE}}^{(e)})_{mp} &= \int_0^d [I'^+_m(x) \hat{x}] \cdot \frac{j}{k_{tp}} [-k_{xp} \hat{y} + k_y \hat{x}] \frac{e^{-jk_{xp}x}}{\sqrt{d}} dx = \\
 &= j \frac{k_y}{k_{tp}} \int_0^d I'^+_m(x) \frac{e^{-jk_{xp}x}}{\sqrt{d}} dx = j \frac{k_y}{k_{tp}} \sum_n I'^+_{mn} \frac{1}{d} \int_0^d e^{-j(k_{xp} - \xi_n)x} dx = j k_y \underline{I}'_+ \text{diag}\left\{ \frac{1}{k_{tp}} \right\} \quad (2.56)
 \end{aligned}$$

$$\begin{aligned}
 (\underline{T}_{\underline{GTMFTM}}^{(e)})_{mp} &= \int_0^d [I'^+_m(x) \hat{x}] \cdot \frac{j}{k_{tp}} [k_{xp} \hat{x} + k_y \hat{y}] \frac{e^{-jk_{xp}x}}{\sqrt{d}} dx = \\
 &= j \frac{k_{xp}}{k_{tp}} \int_0^d I'^+_m(x) \frac{e^{-jk_{xp}x}}{\sqrt{d}} dx = j \frac{k_{xp}}{k_{tp}} \sum_n I'^+_{mn} \frac{1}{d} \int_0^d e^{-j(k_{xp} - \xi_n)x} dx = j \frac{k_{xp}}{k_{tp}} I'^+_m = j \underline{I}'_+ \text{diag}\left\{ \frac{k_{xp}}{k_{tp}} \right\} \quad (2.57)
 \end{aligned}$$

The next step is the construction of second projection matrix $\underline{T}_{FG}^{(h)}$, according to the last equation of (2.49), i.e. that one related to the junction having homogeneous halfspace on the left (F) and grating on the right (G) (i.e. at $z = 0$). Before doing that, it is important to highlight which modes have to be used, as already did in (2.52) in the G-F case.

$$\begin{cases} \hat{z} \times \underline{e}'_{Fp} = \frac{j}{\sqrt{d}} [-\frac{k_{xp}}{k_{tp}} \hat{y} + \frac{k_y}{k_{tp}} \hat{x}] e^{jk_{xp}x} \\ \hat{z} \times \underline{e}''_{Fp} = \frac{j}{\sqrt{d}} [-\frac{k_{xp}}{k_{tp}} \hat{x} - \frac{k_y}{k_{tp}} \hat{y}] e^{jk_{xp}x} \\ \underline{h}'_{Gm} = I'_n(x) \hat{y} \\ \underline{h}''_{Gm} = [-V''_m(x) \hat{x} + Z''_{Gm} I''_m(x) \frac{k_y}{k_{tp}} \hat{y}] \end{cases} \quad (2.58)$$

Exactly in as the previous case, the projection matrix is four times greater than the case analysed in Section 2.1.1, where only TE polarization have been considered during projection, as highlighted in red in (2.59). Clearly, $k_y = 0$ condition would simplify the projection matrix in that case, but general incidence is actually considered in this case.

$$\underline{\underline{T}}_{FG}^{(h)} = \begin{bmatrix} \underline{\underline{T}}_{FTEGTE}^{(h)} & \underline{\underline{T}}_{FTEGTM}^{(h)} \\ \underline{\underline{T}}_{FTMGTE}^{(e)} & \underline{\underline{T}}_{FTMGTM}^{(e)} \end{bmatrix} \quad (2.59)$$

Such as in the G-F case, scalar products aimed to find all four matrices of (2.59) have been developed below, considering now (2.58).

$$\begin{aligned} (\underline{\underline{T}}_{FTEGTE}^{(h)})_{pm} &= \int_0^d \frac{j}{k_{tp}} [-k_{xp}\hat{x} - k_y\hat{y}] \cdot [-V_m''(x)\hat{x} + Z_{Gm}'' I_m''(x) \frac{k_y}{k_{zm}''} \hat{y}] \frac{e^{jk_{xp}x}}{\sqrt{d}} dx = \\ &= j \frac{k_{xp}}{k_{tp}} \int_0^d V_m''(x) \frac{e^{jk_{xp}x}}{\sqrt{d}} dx - j \frac{Z_{Gm}'' k_y^2}{k_{zm}'' k_{tp}} \int_0^d I_m''(x) \frac{e^{jk_{xp}x}}{\sqrt{d}} dx = \\ &= j \frac{k_{xp}}{k_{tp}} \sum_n V_{mn}'' \frac{1}{d} \int_0^d e^{-j(\xi_n - k_{xp})x} dx - j \frac{Z_{Gm}'' k_y^2}{k_{zm}'' k_{tp}} \sum_n I_{mn}'' \frac{1}{d} \int_0^d e^{-j(\xi_n - k_{xp})x} dx = \\ &= j \frac{k_{xp}}{k_{tp}} V_{mp}'' - \frac{Z_{Gm}'' k_y^2}{k_{zm}'' k_{tp}} I_{mp}'' = j(\underline{\underline{V}}'' \text{diag}\{\frac{k_{xp}}{k_{tp}}\})^T - j k_y^2 (\text{diag}\{\frac{Z_{Gm}''}{k_{zm}''} \underline{\underline{I}}'' \text{diag}\{\frac{1}{k_{tp}}\})^T \end{aligned} \quad (2.60)$$

$$\begin{aligned} (\underline{\underline{T}}_{FTMGTE}^{(h)})_{pm} &= \int_0^d \frac{j}{k_{tp}} [k_y\hat{x} - k_{xp}\hat{y}] \cdot [-V_m''(x)\hat{x} + Z_{Gm}'' I_m''(x) \frac{k_y}{k_{zm}''} \hat{y}] \frac{e^{jk_{xp}x}}{\sqrt{d}} dx = \\ &= -j \frac{k_y}{k_{tp}} \int_0^d V_m''(x) \frac{e^{jk_{xp}x}}{\sqrt{d}} dx - j \frac{Z_{Gm}'' k_y k_{xp}}{k_{zm}'' k_{tp}} \int_0^d I_m''(x) \frac{e^{jk_{xp}x}}{\sqrt{d}} dx = \\ &= -j \frac{k_y}{k_{tp}} \sum_n V_{mn}'' \frac{1}{d} \int_0^d e^{-j(\xi_n - k_{xp})x} dx - j \frac{Z_{Gm}'' k_y k_{xp}}{k_{zm}'' k_{tp}} \sum_n I_{mn}'' \frac{1}{d} \int_0^d e^{-j(\xi_n - k_{xp})x} dx = \\ &= -j \frac{k_y}{k_{tp}} V_{mp}'' - \frac{Z_{Gm}'' k_y k_{xp}}{k_{zm}'' k_{tp}} I_{mp}'' = -j k_y (\underline{\underline{V}}'' \text{diag}\{\frac{1}{k_{tp}}\})^T - j k_y (\text{diag}\{\frac{Z_{Gm}''}{k_{zm}''} \underline{\underline{I}}'' \text{diag}\{\frac{k_{xp}}{k_{tp}}\})^T \end{aligned} \quad (2.61)$$

$$\begin{aligned}
 (\underline{T}_{FTEGTM})_{pm} &= \int_0^d \frac{j}{k_{tp}} [-k_{xp}\hat{x} - k_y\hat{y}] \cdot [I'_m(x)\hat{y}] \frac{e^{jk_{xp}x}}{\sqrt{d}} dx = \\
 -j \frac{k_y}{k_{tp}} \int_0^d I'_m(x) \frac{e^{jk_{xp}x}}{\sqrt{d}} dx &= -j \frac{k_y}{k_{tp}} \sum_n I'_{mn} \frac{1}{d} \int_0^d e^{-j(\xi_n - k_{xp})x} dx = \\
 -j \frac{k_y}{k_{tp}} I'_{mp} &= -j k_y (\underline{I}' \text{diag}\{\frac{1}{k_{tp}}\})^T
 \end{aligned} \tag{2.62}$$

$$\begin{aligned}
 (\underline{T}_{FTMGTM})_{pm} &= \int_0^d \frac{j}{k_{tp}} [k_y\hat{x} - k_{xp}\hat{y}] \cdot [I'_m(x)\hat{y}] \frac{e^{jk_{xp}x}}{\sqrt{d}} dx = \\
 -j \frac{k_{xp}}{k_{tp}} \int_0^d I'_m(x) \frac{e^{jk_{xp}x}}{\sqrt{d}} dx &= -j \frac{k_{xp}}{k_{tp}} \sum_n I'_{mn} \frac{1}{d} \int_0^d e^{-j(\xi_n - k_{xp})x} dx = \\
 -j \frac{k_{xp}}{k_{tp}} I'_{mp} &= -j (\underline{I}' \text{diag}\{\frac{k_{xp}}{k_{tp}}\})^T
 \end{aligned} \tag{2.63}$$

At this point, projection matrices related to the two wave guide junctions have been achieved (always referring to the scheme of Figure 2.2), therefore equations related to the continuity conditions at $z = 0$ and $z = z_0$ already developed in section 2.1.1 can be expressed even using both $\underline{T}_{GF}^{(e)} = T$ and $\underline{T}_{FG}^{(h)} = T^+$.

Chapter 3

Simulations related to the diffraction grating behaviour

Formulation related to the rigorous coupled-wave analysis (RCWA) has been carried out analytically in the previous chapter.

First of all, the simplest case of plane wave as incident wave has been illustrated in section 3.1 in order to achieve the scattering parameters of a diffraction grating of infinite extent. Related to this, the first step concerning the simulation was to define the geometry of the structure required during the analysis, together with the parameters of the whole system (wavelength under analysis, refractive indexes, incident angle and so on).

Even the number of the Floquet modes involved in the analysis as been setted previously, since the number of harmonics must be evaluated. Then, the calculation of the Floquet indexes and therefore the modal expansions have been achieved by means the evaluation of the $\underline{\mathbf{E}}$ matrix.

Successively, a function related to the evaluation of PSWW modes has been built, proceeding exactly as it has been already shown in Section 2.2 of the previous chapter. After that, the reconstruction of the grating dielectric profile has been performed by using the expansion of the Floquet modes in order to check the aforementioned matrix.

The evaluation of eigenvectors has been made by simply using the *eig* function, that is already provided by MATLAB®. The last steps concern the evaluation of the scattering parameters by means the mode matching technique shown in 2.1.1. For simplicity, both half spaces have been considered with the same refractive index $n_{IN} \approx 1$ (air). Some plots concerning the scattered fields have been plotted in order to analyse grating behaviour. All of what has been written for the plane wave just before has been performed even in the more realistic case in section 3.2, where a Gaussian Beam is employed as source.

3.1 Grating excited by a plane wave

The first case analysed consists, as already written before, to a plane wave incident from the left (exactly as shown in Figure 2.1 of Chapter 2). The plane wave has, according to its definition, infinite extended wave fronts whose hit uniformly each unit cell of the grating. The choice to simulate the device stimulated by this kind of incident wave allows to directly plot the scattering parameters of the simulated grating. To better understand how the scattering parameters are produced, some concepts about the "signal theory" are used. Considering the system under analysis like in Figure 3.1:

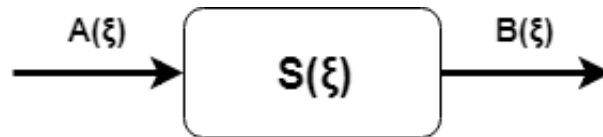


Figure 3.1: Block representing the system by means its equivalent scattering matrix.

$A(\xi)$ represents the spatial Fourier transform of the input stimulus, i.e. the plane wave having a unitary spatial spectrum. For this reason, assuming the system under analysis as a linear time-invariant (LTI) one, the output $B(\xi)$ (which represents in this case the scattered contributions of the device) gives the exact contribution of the scattering parameters.

$$B(\xi) = A(\xi)\mathbf{S}(\xi) = \mathbf{S}(\xi) \quad (3.1)$$

For what concerns the MATLAB® code, all steps described in the introduction of this chapter has been written in the latter. For the simulation process, here are all data related to the structure parameters and geometry.

```

1 %%%%%%%%%%%%%%%%%%%%%%%%%%%%%%%%%%%%%%%%%%%%%%%%%%%%%%%%%%%%%%%%%%%%%%%%%
2 % Geometry of the structure
3 %%%%%%%%%%%%%%%%%%%%%%%%%%%%%%%%%%%%%%%%%%%%%%%%%%%%%%%%%%%%%%%%%%%%%%%%%
4 %-- Global structure parameters
5 Geometry.n_in=1; %-- Refractive index left/right half-spaces
6 Geometry.Lambda=1600; %-- Period of the structure, nm
7 Geometry.n1=3.214; %-- Refractive index of the bar
8 Geometry.n2=1; %-- Refractive index of the bar surrounding material
9 Geometry.tg=220; %-- Grating thickness, nm
10 Geometry.eta=0.5; %-- Filling factor of the grating bars (from 0 to 1)
11 %
12 %%%%%%%%%%%%%%%%%%%%%%%%%%%%%%%%%%%%%%%%%%%%%%%%%%%%%%%%%%%%%%%%%%%%%%%%%
13 % Parameters of the program
14 %%%%%%%%%%%%%%%%%%%%%%%%%%%%%%%%%%%%%%%%%%%%%%%%%%%%%%%%%%%%%%%%%%%%%%%%%
15 Parameters.theta=-10; % plane-wave incidence angle, degrees
16 Parameters.lambdavet=linspace(1200,3200,105); % wavelengths vector, nm
17 %
18 %-- ALWAYS ODD numbers (generation of Floq. modes)
19 Parameters.NModes=15; %-- inner half-space
20 Parameters.NHarmonicsTE=2*Parameters.NModes+1; %-- Harmonics used to build TE ↔
    PSWW modes
21 %
22 %%%%%%%%%%%%%%%%%%%%%%%%%%%%%%%%%%%%%%%%%%%%%%%%%%%%%%%%%%%%%%%%%%%%%%%%%
23 % Program
24 %%%%%%%%%%%%%%%%%%%%%%%%%%%%%%%%%%%%%%%%%%%%%%%%%%%%%%%%%%%%%%%%%%%%%%%%%
25 theta=Parameters.theta*pi/180; % conversion of degrees to radians

```

Figure 3.2: Input data for this first simulation.

Indexes of Floquet modes have been evaluated and used to establish all the harmonics related to the entire high-order modes. The expansions of the Floquet modes have been even employed to reconstruct the dielectric profile of a single cell composed by a bar and having a period Λ (*Geometry.Lambda* in the code of Figure 3.2), according to (2.39) of section 2.1.2. This step is useful to check the correctness of $\underline{\underline{E}}$ matrix.

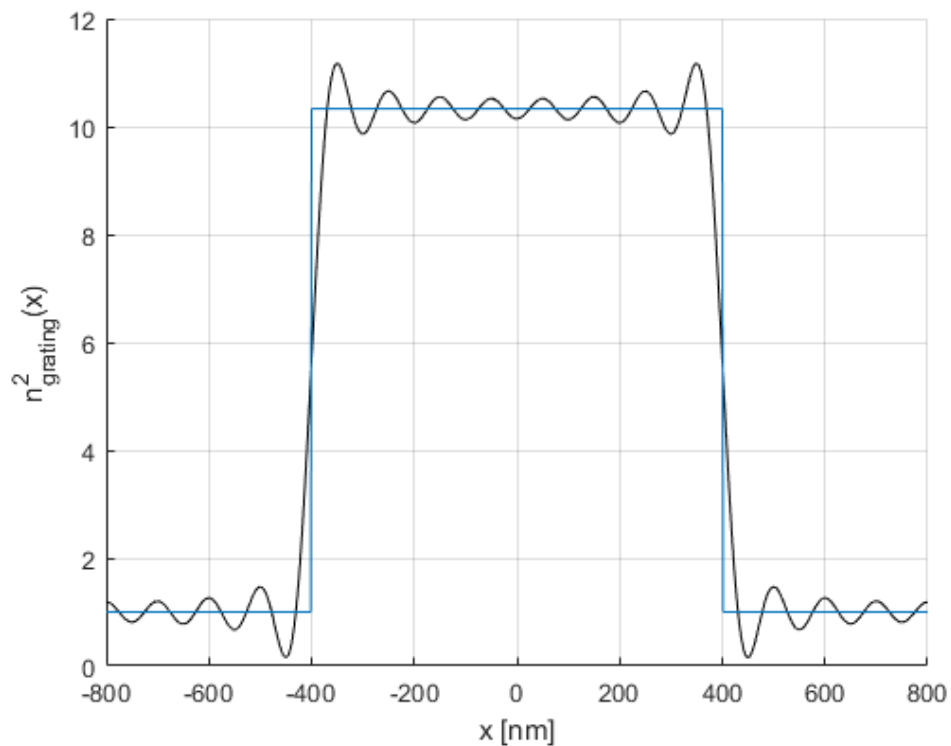


Figure 3.3: Exact (black line) and reconstructed (blue line) unit cell dielectric profile $n^2(x)$.

Observing Figure 3.3, it is clear how the number of Floquet mode setted in the code of Figure 3.2 is linked to x_i and hence it influences the resolution of reconstructed profile used in RCWA. Indeed, this fact is provable increasing from 15 to 75 the value *Parameters.NModes*.

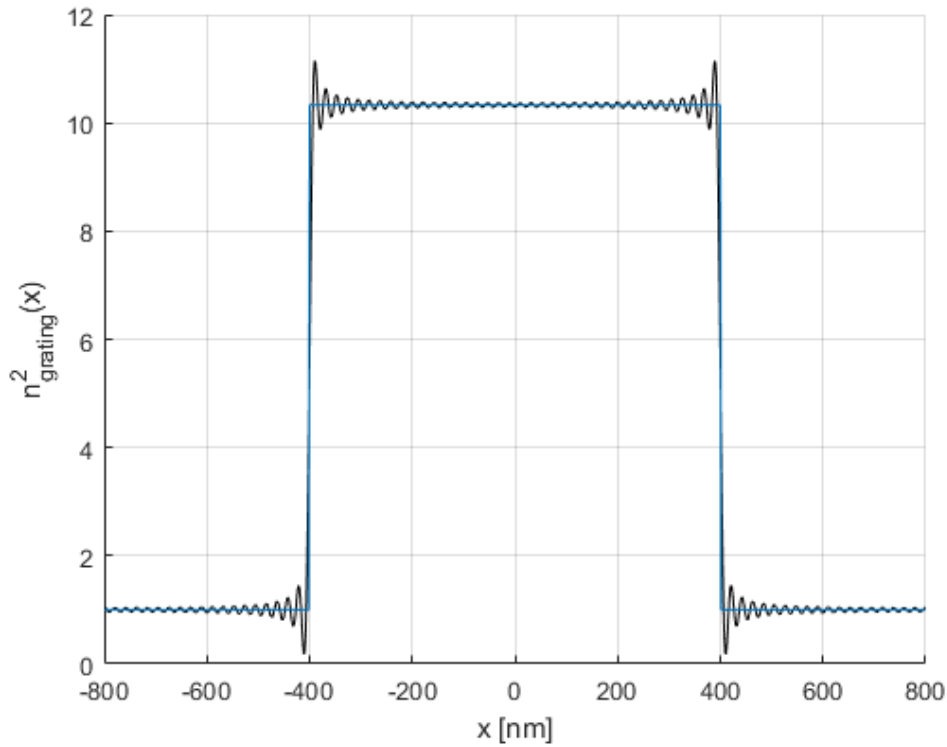


Figure 3.4: Exact (black line) and reconstructed (blue line) unit cell dielectric profile $n^2(x)$, with a number of 75 selected modes.

Clearly, the reconstructed profile approaches to the exact one increasing the number of involved modes, since there are actual more harmonics to sum together in order to better approximate the ideal profile. Nevertheless, limited calculation capability of the simulator represents a constraint of selected number of modes.

Afterwards, reflectivity (S_{11}^2) of the dielectric device has been plotted according to the range of inserted input wavelength. For each of them, the program performs a calculation concerning the evaluation of the scattering parameter at that input frequency.

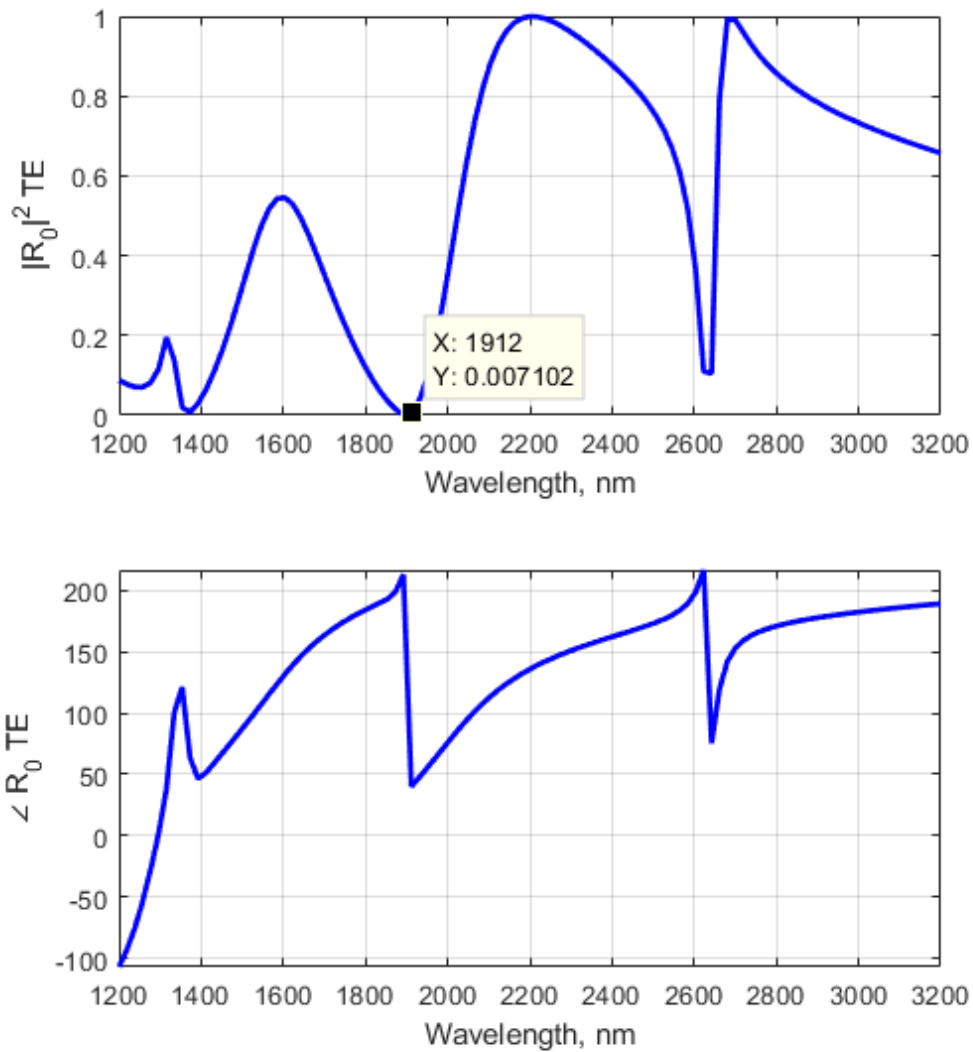
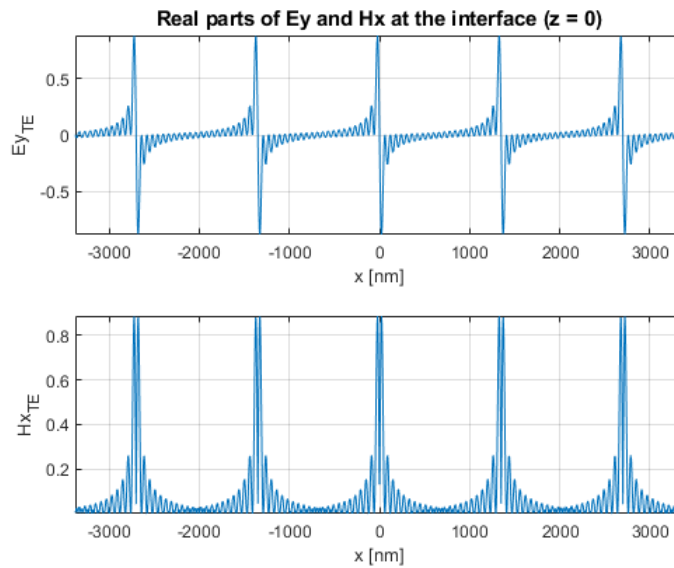
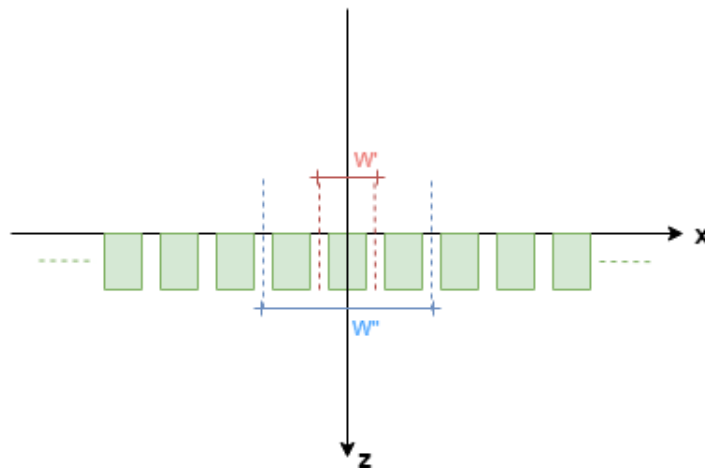


Figure 3.5: Reflectivity and S_{11} phase evaluated for each provided input wavelength.

With the settings of Figure 3.2, the diffraction grating is "transparent" at a wavelength of about 1900 nm, while it behaves like a mirror both at 2200nm and 2700nm of λ , respectively. Using the latter value as input wavelength, it is interesting to observe how the fields of TE mode behaves at ($z = 0$).

Figure 3.6: Electric and magnetic field at $z = 0$.

Both E_y and H_x have been found in this script according to the calculations made in (2.37), considering the continuity conditions at the interfaces. The most interesting stuff of Figure 3.6 consists to the recognition of zones where bars are presents. In other words, these fields track the grating "shadow" considering each unit cell composed as Figure 3.4. Coming back to the reflectivity of Figure 3.5, it has been used even to prove the concept already exposed in the section 2.1.2. Instead to construct an elementary cell having a single bar, three bars has been considered now, imaging to maintain the same periodic structure as illustrated in Figure 3.7.

Figure 3.7: Infinite gratings under analysis, with the case of single bar per cell (red period W') and three bars per cell (blue period W'').

Since the dielectric grating has been described by fixing periodic boundary conditions

for an elementary cell, the value of ξ changes according to period. Indeed, reporting the ξ form from (2.2), it is clear how the mode expansions better fit the ideal index profile when cell period is lowered and the number of involved Floquet modes m are increased. The direct proportion of these two factors in ξ is quite visible even in the proof of Figure 3.8, where the number of modes has been tripled in order to compensate the greater cell period.

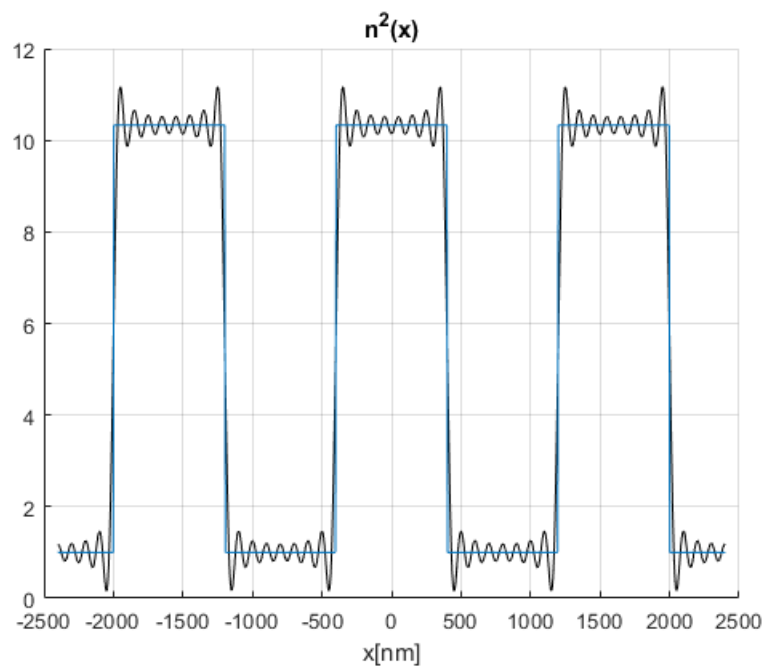


Figure 3.8: Reconstruction of the dielectric profile in the case of a cell made with three bars.

In the plot above, the number of selected modes is 45 (in contrast to the 15 modes fixed initially in Figure 3.2) such that the reconstructed index profile is the same of the previous case. In order to verify this fact, it is enough to compare the oscillations shown in Figure 3.8 to those ones displayed for the case of Figure 3.3 (even though the x-axis in these two plots has different resolution).

A confirm of what is written before is the plot concerning reflectivity of the structure in Figure 3.9. These curves perfectly matched with those ones of Figure 3.5 (the latter are also included in the plots just below and they are perfectly superimposed by the new reflectivity). These data confirm how the simulated diffraction grating is the same of the first case.

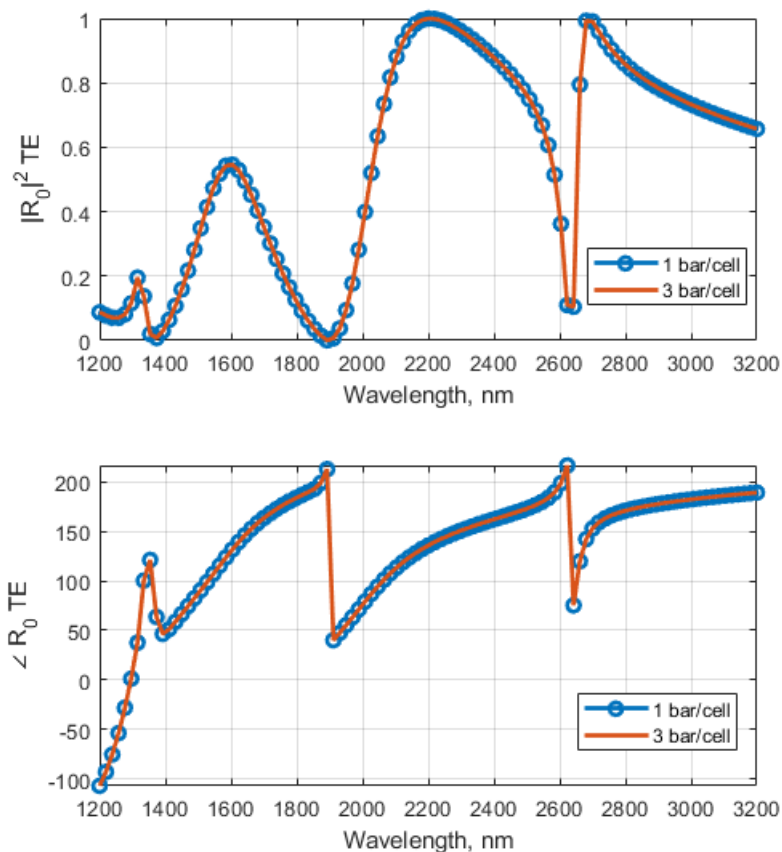


Figure 3.9: Reflectivity plot in the case of an elementary cell composed by three bars, compared to the plot of Figure 3.5.

What really changes with respect to the previous analysis with a single bar per cell are the number of modes staying above cut-off, which is different in the two cases. Considering the Floquet theory [8], high-order modes contribution are distributed in harmonics arranged in a way resembling a rake. The limits such that those high-order modes are above cut-off is $|\xi_m| < k_0$, i.e. their contribution must not be evanescent. Clearly, according to ξ_m evaluated in (2.2), the "teeth of the rake" are going to be closer one to each others if the period W is greater. Concluding, this fact means that there are an higher number of modes above cut-off in the last case.

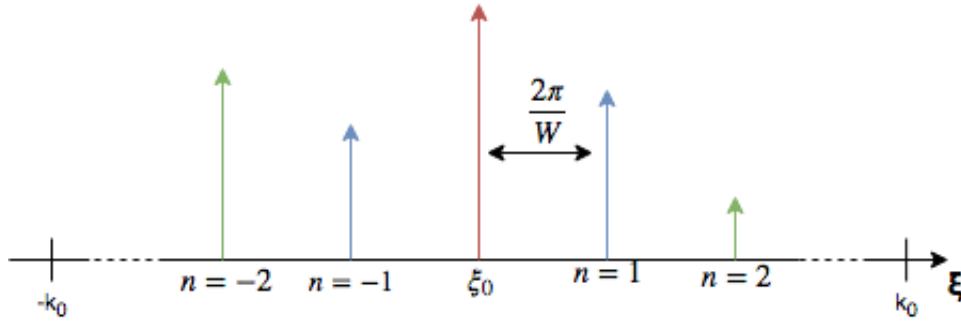


Figure 3.10: Example of spatial Fourier transform representing harmonics associated to the high-order modes.

The number of modes above cut-off can be shown in the MATLAB® script by observing the number of real $k_{zm} = \sqrt{k_0^2 n_{IN}^2 - (\frac{2\pi m}{W})^2}$ in the homogeneous space.

<pre>>> HalfSpaceInfo.kz ans = 0.0019 + 0.0000i 0.0000 - 0.0038i 0.0000 - 0.0030i 0.0000 - 0.0080i 0.0000 - 0.0073i 0.0000 - 0.0120i 0.0000 - 0.0113i 0.0000 - 0.0159i 0.0000 - 0.0152i 0.0000 - 0.0199i 0.0000 - 0.0192i 0.0000 - 0.0238i 0.0000 - 0.0231i 0.0000 - 0.0278i 0.0000 - 0.0271i</pre>	<pre>>> HalfSpaceInfo.kz ans = 0.0019 + 0.0000i 0.0011 + 0.0000i 0.0017 + 0.0000i 0.0000 - 0.0022i 0.0000 - 0.0012i 0.0000 - 0.0038i 0.0000 - 0.0030i 0.0000 - 0.0052i 0.0000 - 0.0045i 0.0000 - 0.0066i 0.0000 - 0.0059i 0.0000 - 0.0080i 0.0000 - 0.0073i 0.0000 - 0.0093i 0.0000 - 0.0086i</pre>
---	---

Figure 3.11: k_z values referred to the case of a cell with single bar(left) and three bars (right), respectively.

A "rake" three times denser than one bar per cell case allows in the latter structure to get triple modes above cut-off. However, the choice of using a cell composed by several bars requires an augment of selected Floquet modes in the half spaces in order to maintain a good modal expansions (verified by reconstructing the dielectric profile), but in that case the simulation requires more computation costs.

Nevertheless, as explained in the thesis introduction, a single cell composed with several bars followed by a long material with constant refractive index is employed in the next section in order to simulate the behaviour of a possible grating with finite extent.

3.2 Grating excited by a Gaussian beam

Until now, plane wave has been used as incident source mainly in order to highlight how scattering parameters change according to the input wavelength. In this section, a Gaussian beam is used as incident wave because it represents a more realistic source.

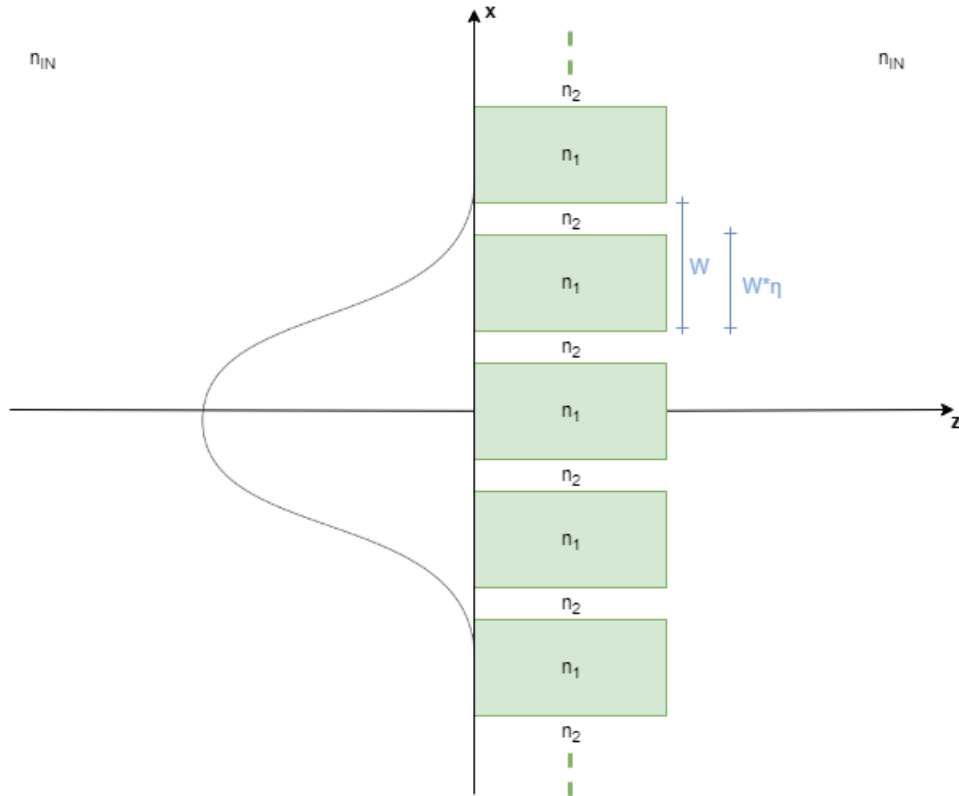


Figure 3.12: Gaussian beam illuminating the dielectric grating.

Starting from a brief description of the Gaussian beam, it is a "bell curve" signal mainly characterized by both an amplitude (considered unitary for simplicity) and a beam waist w .

$$A(x) = e^{-\frac{x^2}{w^2}} \quad (3.2)$$

Using the same nomenclature of (3.1), now the "output" of the system shows even information about the input. Nevertheless, the rigorous couple-wave analysis does not change, but now the spatial Fourier transform of the input signal influences the output one.

$$A(x) = \frac{1}{2\pi} \int A(\xi) e^{-j\xi x} d\xi \rightarrow A(\xi) = w\sqrt{\pi} e^{-\frac{w^2 \xi^2}{4}} \quad (3.3)$$

Scattering parameters have been calculated using again the same approach of the plane wave, but in this case the choice to fix a single input wavelength has been taken in order to make lighter the MATLAB® execution. RCWA is still applicable because a Gaussian Beam can be seen as a group of plane waves having different incident angles theta, therefore the previous script is performed several times for every value of the aforementioned angles. Considering for instance the contribution resulted by the reflection (S_{11}) of the Gaussian beam, it has been calculated as follow:

$$B(x) = \sum_n \sum_{\vartheta} A(\vartheta) S_{11}(\vartheta) e^{-j\xi_n x} \quad (3.4)$$

Where the n subscript refers to the number of selected Floquet modes. Besides, theta dependency of the spatial Fourier transform of the Gaussian beam $A(\xi)$ has been highlighted remembering that the incident angle and the x component of the wave number are correlated.

$$\xi = k_x = k_0 n_{IN} \sin(\vartheta) \quad (3.5)$$

Just for completeness, a bell curve with a beam waist of $20\mu m$ and its SFT have been plotted in Figure 3.13 (input parameters remained those ones in Figure 3.2, with a single input wavelength of 3400 nm selected). It is possible to observe how the spatial Fourier transform in theta domain is limited to $\pm \frac{\pi}{2}$ due to the sine presence in (3.5), which correspond to the limit $|\xi_m| < k_0$ already seen in section 3.1 and marked in Figure 3.10, which defines modes above cut-off.

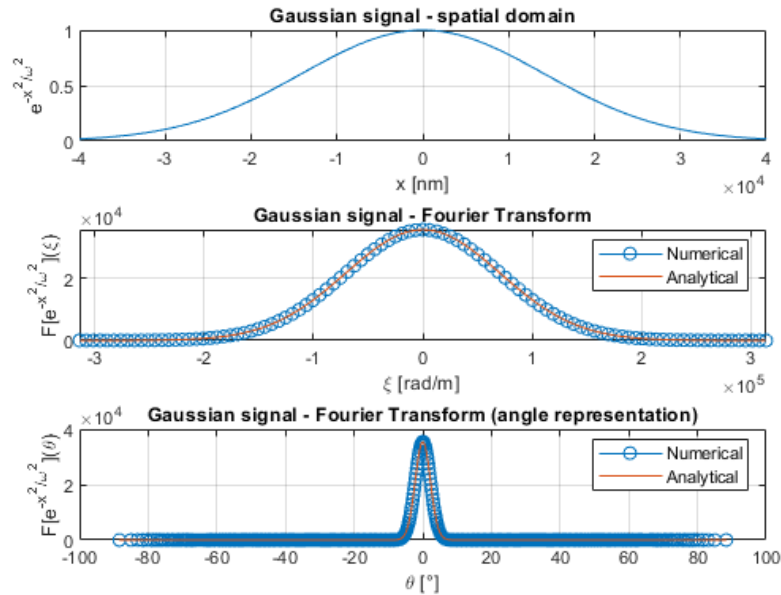


Figure 3.13: Gaussian beam signal (top) and its Spatial Fourier Transform expressed both in ξ (middle) and ϑ (bottom) domains.

In Figure 3.13 the Fourier Transform has been calculated both analytically and performing a FFT (numerically) as proof, with the latter introducing a certain resolution. By the way, this curve is the $A(\xi)$ of (3.4), hence it is possible to study the results provided by the scattering simply multiplying this spectrum with the scattering parameters defined for each ϑ considering a simulated diffraction grating composed by periodic cell having a single bar, as Figure 3.3.

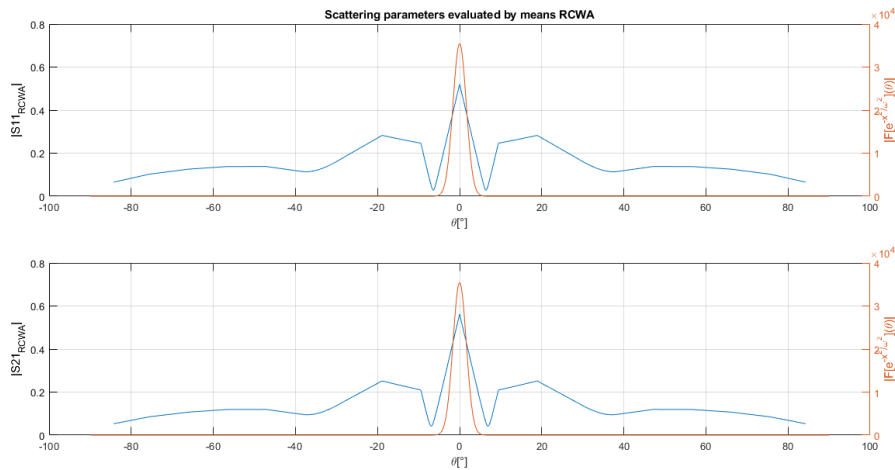


Figure 3.14: Spatial Fourier Transform of the Gaussian curve versus the evaluated scattering parameters for each theta.

As first approach, only the weight of the scattered fundamental mode has been analysed, hence the reflected and transmitted electric fields related to it has been plotted in Figure 3.15. The generation of these data has been obtained by performing a inverse Fast Fourier Transform (iFFT).

3. Simulations related to the diffraction grating behaviour

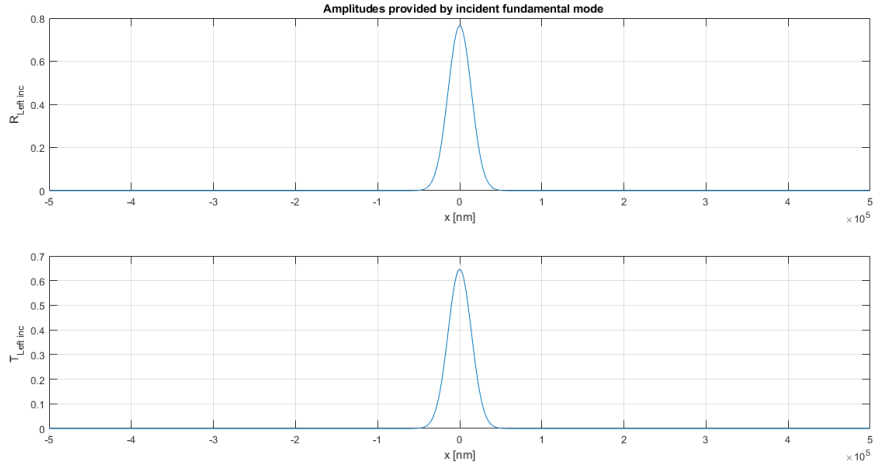


Figure 3.15: Reflected (top) and transmitted (bottom) fundamental mode contribution (in module) by the dielectric grating, considering fundamental mode of the Gaussian Beam in Figure 3.13 the only incident one.

The plots of Figure 3.15 do not consider the scattered parts related to the others modes, though. In order to take them into account, it is necessary to evaluate both for each Floquet mode and thetas the respective scattering parameters and then summing the entire contributions together according to (3.4), exploiting the linear properties of the spatial Fourier Transform. The FLOQMAT matrix already expressed at the end of section 2.1.1 is aimed to both anti-transform and sum the factors just cited before. In Figure 3.16 both reflected and transmitted contribution related to the all high-order modes has been shown, even considering for simplicity the fundamental mode as the only incident one.

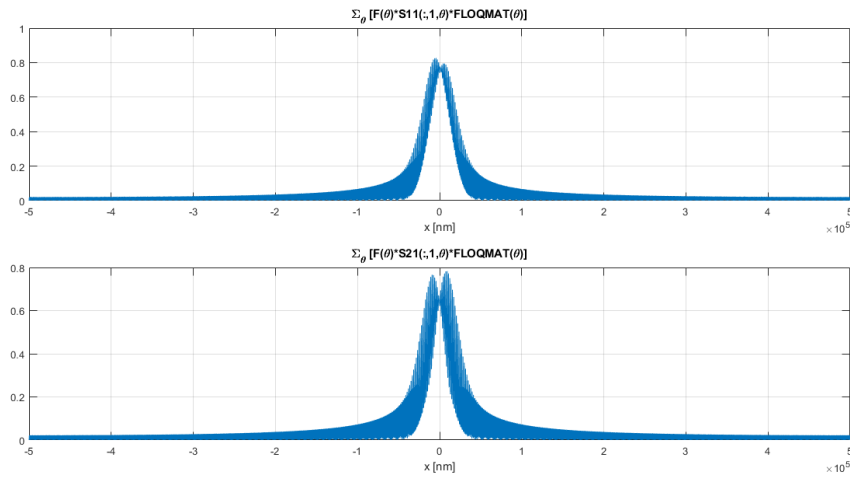


Figure 3.16: Reflected and transmitted contributions considering all modes, studied in the case of fundamental mode taken into account as the only incident one.

The employed Gaussian beam has a waist ($20\mu m$) in this simulation which is more than 12 times the cell period of the diffraction grating. Therefore, what happens is that the incident wave "sees" the dielectric structure like a mirror with an equivalent refractive index (which value depends by both the geometry and refractive indexes of the elementary cells). Both reflected and transmitted fields of Figure 3.16 resemble the bell curve used as input stimulus. Furthermore, it is interesting to observe how the reconstructed fields shown in Figure 3.16 agree the expansion of Floquet modes, as shown in Figure 3.17.

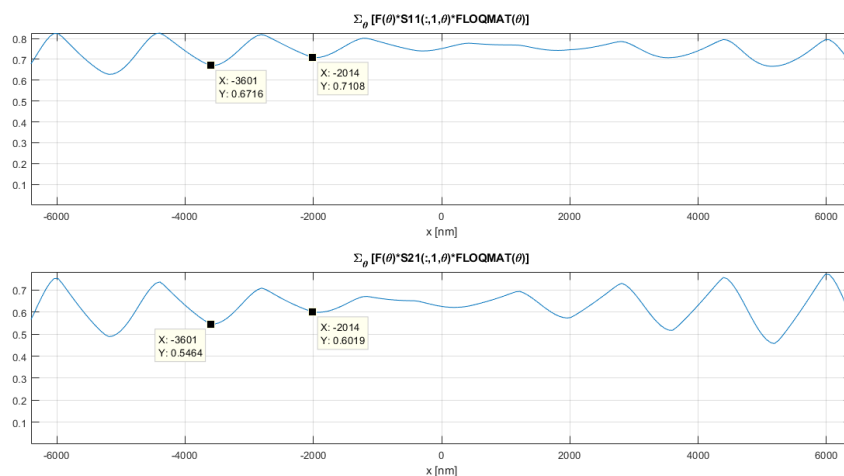


Figure 3.17: Figure 3.16 zoomed from $-6400nm < x < 6400nm$. The cell period of 1600 nm leads the modal expansions.

However, it is important to remember again how the limit $|\xi| < k_0$ states the number of modes above cut-off, i.e. those ones such that k_z is real. On the contrary, the modes below cut-off are associated to imaginary k_z (i.e. to evanescent waves), exactly as in the case of a dielectric wave guide[9]. Modifying the MATLAB® script related to Figure 3.16 in order to plot the contribution of modes above cut-off only, the scattered contributions related to the diffraction grating of infinite extent with an incident Gaussian beam has been reported in Figure 3.18. The entire set of parameters related to the Geometry has been remained as in the previous case.

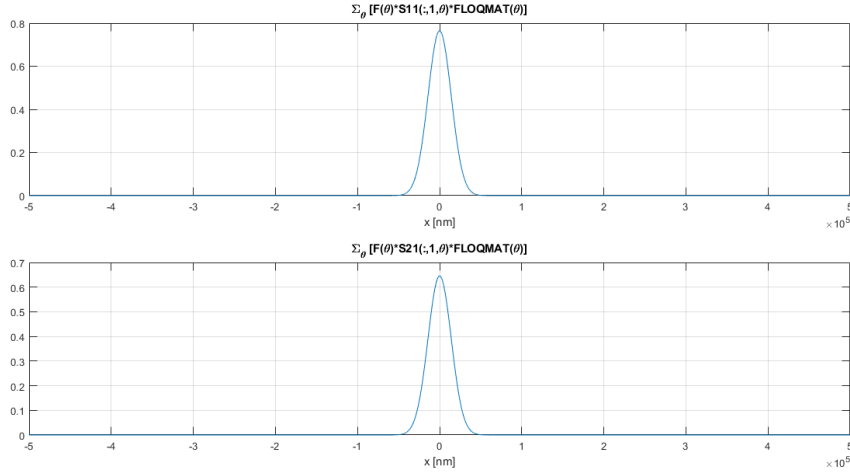


Figure 3.18: Reflected and transmitted contributions considering modes above cut-off only, studied in the case of fundamental mode taken into account as the only incident one.

The case shown just above refers to the condition with a cell composed by a single bar, exactly as Figure 3.3 with a number of 15 modes setted. In that case, it has been shown in Figure 3.11 (left) how there is only one mode above cut-off. Reasonably, it is not a randomness that the plot in Figure 3.18 is exactly the same of that one of Figure 3.15. By the way, when in Figure 3.16 the entire set of modes below cut-off have been even considered, it is clear how the mutual interaction among them allows to get a non-negligible contributions at the reflected and transmitted fields produced by the grating.

Enlarging the number of bars from one to three changing proportionally the quantity of selected modes (exactly like in Figure 3.8), the situation doesn't change since the structure is always the same and the three modes above cut-off combine together to provide the contributions equals to those one shown in Figure 3.18.

The reconstructed dielectric profile resolution is a key point for the purpose of this work, indeed using the same fixed number of modes for the intended long elementary cell simulating the "finiteness" of the device, reconstruction could be really bad. This fact represent a check for $\underline{\underline{E}}$ matrix, hence an index for the reliability of scattering parameters. In order to get a kind of idea about the "resolution" of a unit cell, an analysis of scattered fields is performed changing both the period and the number of Floquet modes in the script. Proceeding step by step, considering firstly a unit cell composed by 11 bars (bar and filler dimensions unaltered) and 99 Floquet modes setted, like in Figure 3.19.

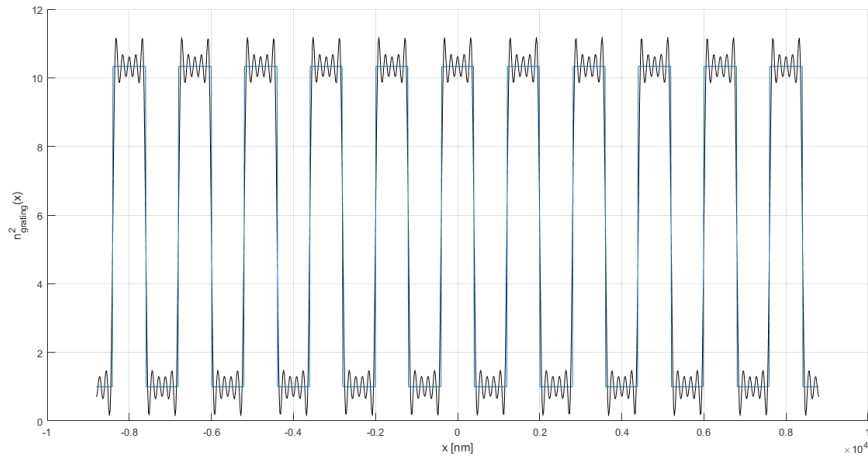


Figure 3.19: Dielectric profile in the case of 11 bars.

The case under analysis is maintained that one of infinite periodic grating, which is used in order to make a comparison with the previous case with the purpose to test the resolution goodness. Observing the results just below, 99 modes in this case are enough to provide a good reconstructed dielectric profile, since the scattered contributions in Figure 3.20 are exactly superimposed to that ones concerning the single bar per cell case previously shown.

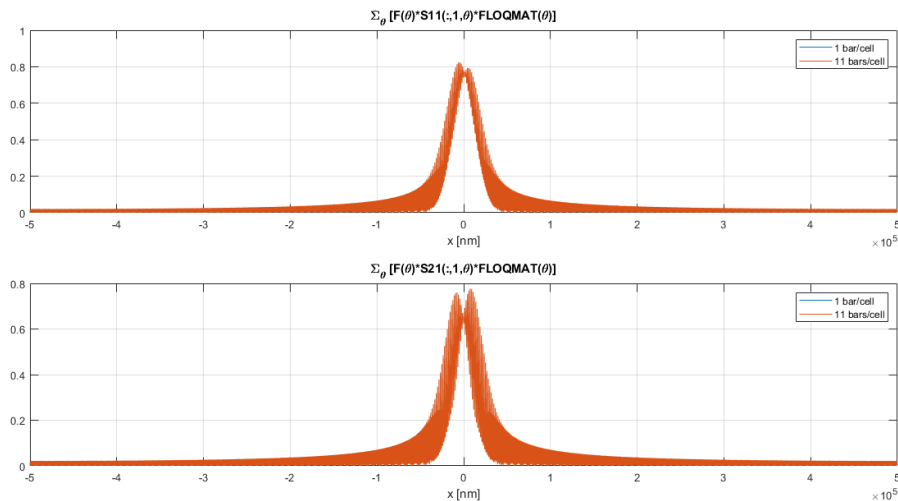


Figure 3.20: Reflected and transmitted contributions in the 11 bars per cell case compared to those one of Figure 3.16.

After analysing the case of infinite grating, the next step is to reconstruct a periodic cell in order to obtain a grating with "fake" finite extents. Now, referring the Gaussian beam of Figure 3.13 which has been employed as source, its waist is clearly the main factor to consider in order to properly size the spacing layers (even called spacers) at

the side of the grating zone aimed to simulate the finiteness of the device (for simplicity, $n_{spacer} = n_{filler} = 1$ during the simulation). A good way to establish a suitable dimension of these "extensions" is by considering negligible the Gaussian contribution at the next cells, where new hypothetical bars would appear.

Supposing the Gaussian beam with a normal incidence at $x=0$ like Figure 1.2, a choice (considering computational costs of simulations) could be to fix the beam intensity of 10% at the cell boundary in order to evaluate consequently the spacers length by the cell period W . Considering meanwhile the scheme in Figure 3.21, a calculation can be done remembering how the cell period (and hence the spacers length) is constrained by the Gaussian waist in order to approach at a simulation of a diffraction grating of finite extent.

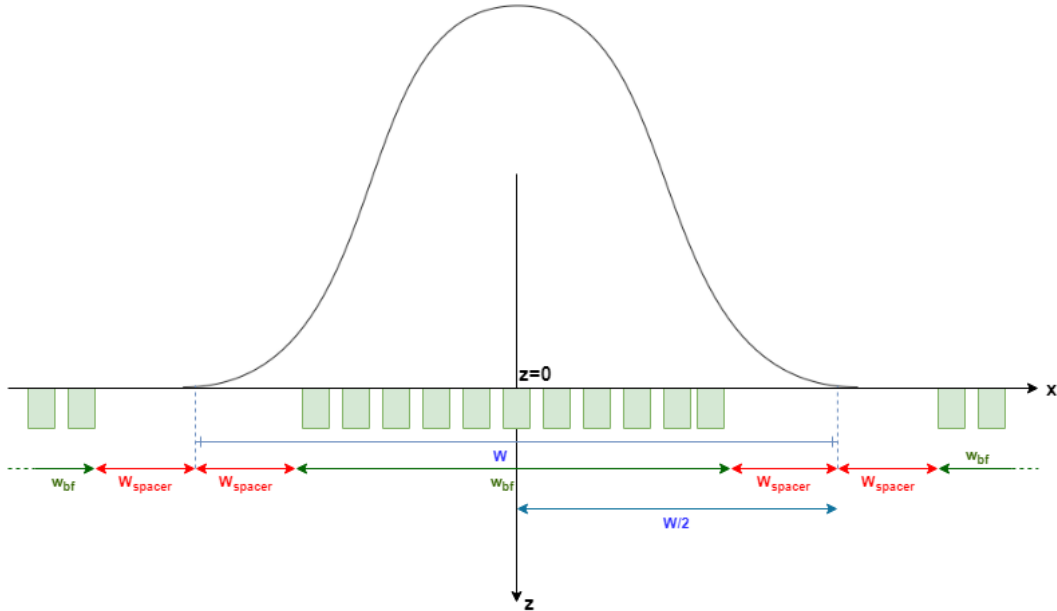


Figure 3.21: Gaussian beam illuminating a single cell composed by 11 bars and two "spacers".

Using the image above, it is possible to state an equation in order to proper design the cell in order to obtain a 10% of intensity at its boundaries, considering the maximum value of the Gaussian beam incident exactly at $x = 0$.

$$e^{-\frac{(W/2)^2}{w^2}} \leq 0.1 \rightarrow W \geq 2w\sqrt{\ln(10)}$$

Finally, spacers are sized according to equation below:

$$W_{spacer} \geq \frac{W - W_{bf}}{2} = w\sqrt{\ln(10)} - \frac{W_{bf}}{2} \quad (3.6)$$

Fixed the bar-to-bar dimension according to the geometries present in code of Figure 3.2 and considering again 11 bars per cell, the grating inside the cell is long $17.6 \mu m$.

The spacers length evaluation is now trivial using (3.6), which yields a value of $21.54\mu m$ (considering that the neighbour cells starts with a spacers, though).

For sake of clarity, a bad case has been reported because it is interesting to see which is the effect of the incident Gaussian beam to the other cells. Starting to fix, for instance, a spacer length of $6\mu m$. Refractive index profile is reconstructed and reported in Figure 3.22 in order to give an idea of the actual unit cell.

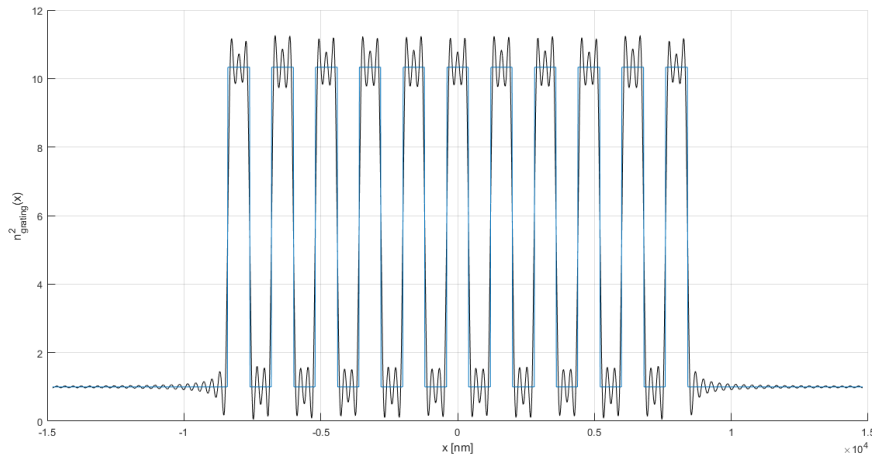


Figure 3.22: Cell dielectric profile composed by 11 bars and 2 spacers long $6\mu m$ at the sides.

Comparing Figure 3.22 with the Gaussian beam of Figure 3.13, it is clear how the incident wave illuminates over the "spacers" zone in a significant manner, even arriving to the bars of the other cells like illustrated in Figure 3.23.

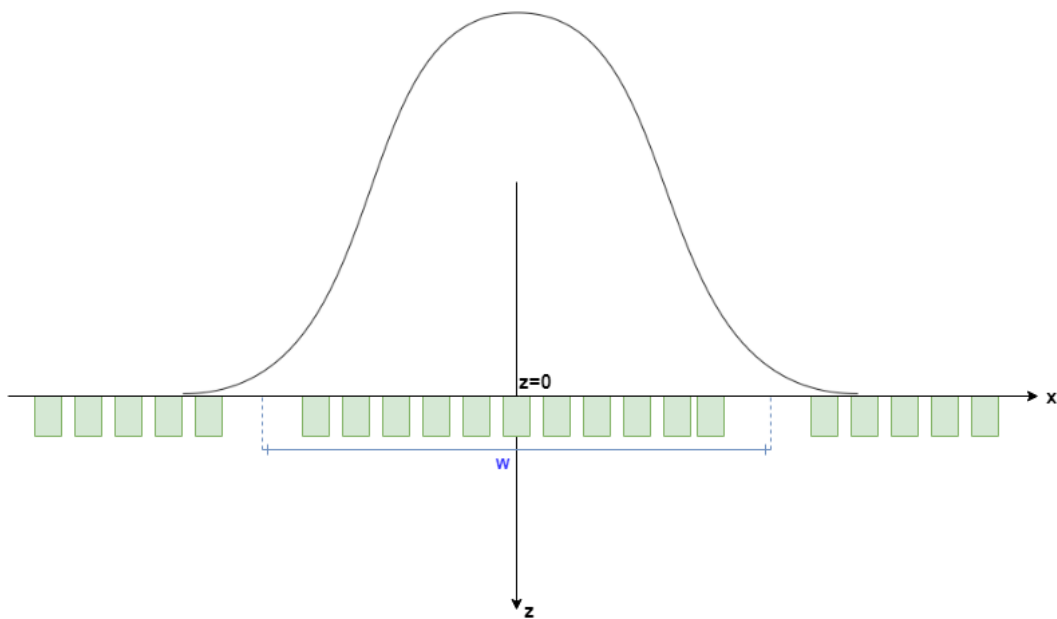


Figure 3.23: Gaussian source illuminating also bars of neighbour cells due to the spacer shortness.

The fact to illuminate even the neighbour cells brings the device to behave in a similar way to the case of grating with infinite periodic structure of Figure 3.16, where scattered contributions resemble something similar to a bell curve, but with distortions related to the spacers presence.

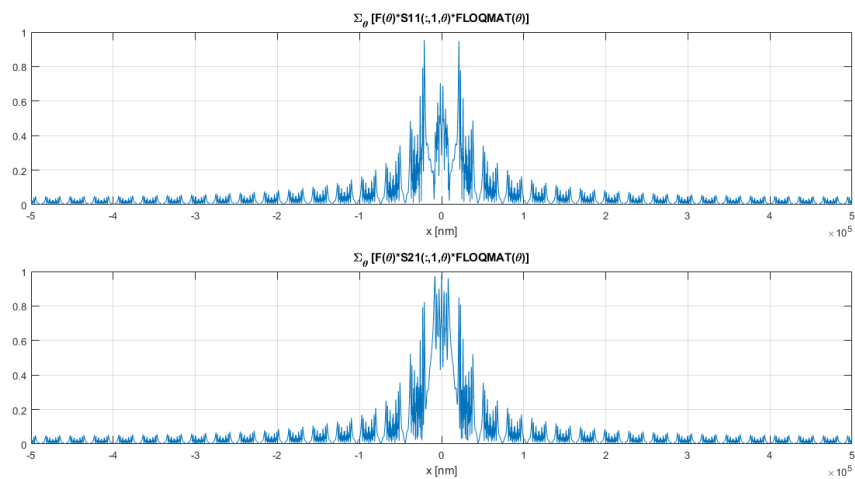


Figure 3.24: Reflected and transmitted contribution employing an elementary cell as Figure 3.22.

Furthermore, it is interesting to analyse how the fixed periodic boundary conditions (and therefore the Floquet modes) characterize the shapes in Figure 3.24, in particular

this fact is more clear in the "tails zone". Zooming for instance in the spatial range of $x = 30\mu\text{m}$, both reflected and transmission contributions have null points after a cell period W (taking into account the MATLAB® data cursor resolution in Figure 3.25), agreeing to the stated boundary condition.

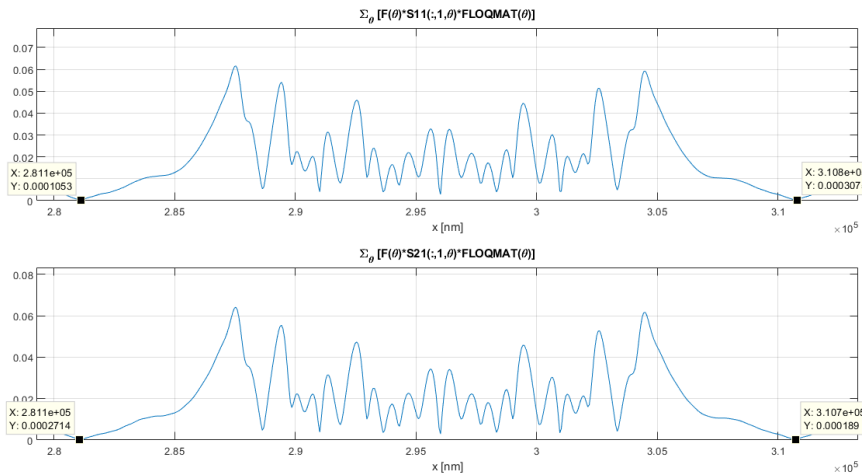


Figure 3.25: Contribution of Figure 3.24, with a zoom at about $30\mu\text{m}$.

Setting now the spacer length to $25\mu\text{m}$ according (3.6), the incident wave affects even less the neighbour cells. In this case, since the period is much greater than before, an heavy calculation has been performed employing 151 modes. Just for comparison, the reconstructed dielectric profiles both in this case and in the case of 99 modes have been plotted below. It is clear how in the case with less modes in Figure 3.26, reconstructed bars degenerates in curved shapes.

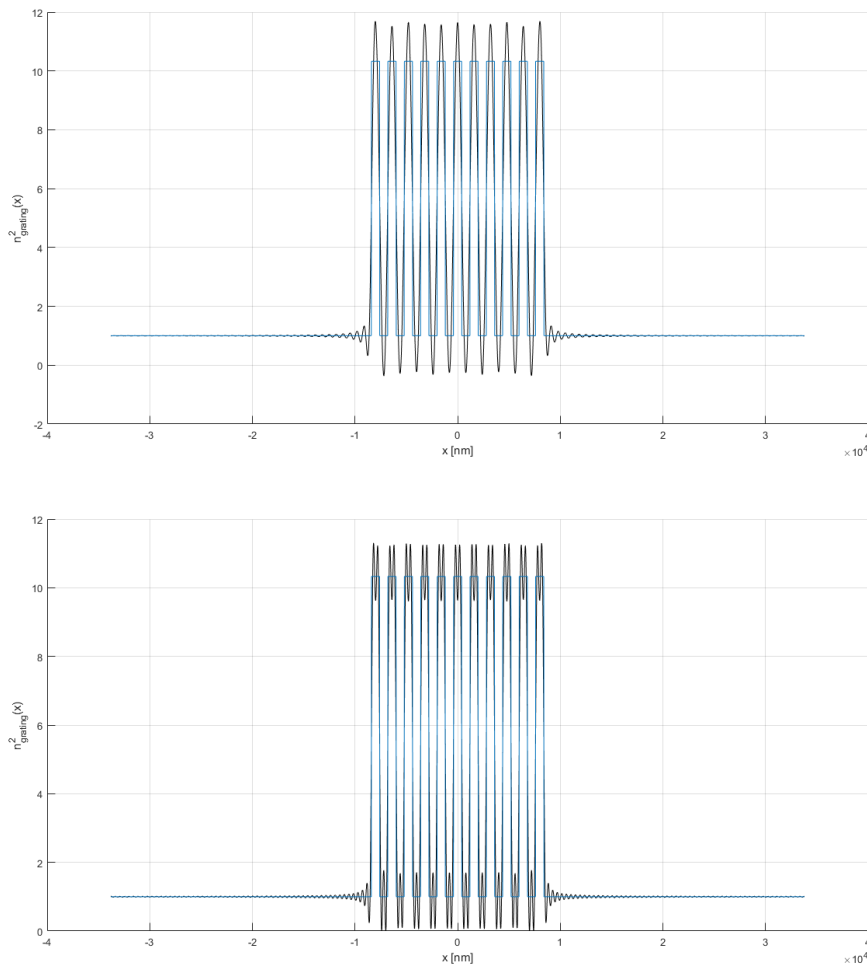


Figure 3.26: Reconstructed dielectric profile of the cell with 99 modes (top) and 151 modes (bottom).

Even employing as source a bell curve with $20\mu\text{m}$, the situation changes with respect to before. The periodic boundary conditions still lead the behaviour of the scattered contributions provided by the grating, but the results are more distorted than before since the Gaussian beam hit only in a little part the region in which the grating is present, hence the bell curve shape tends to get lost in plots of Figure 3.27. According to the wider period, even the contributions at the tails proximity are sparser than the previous case.

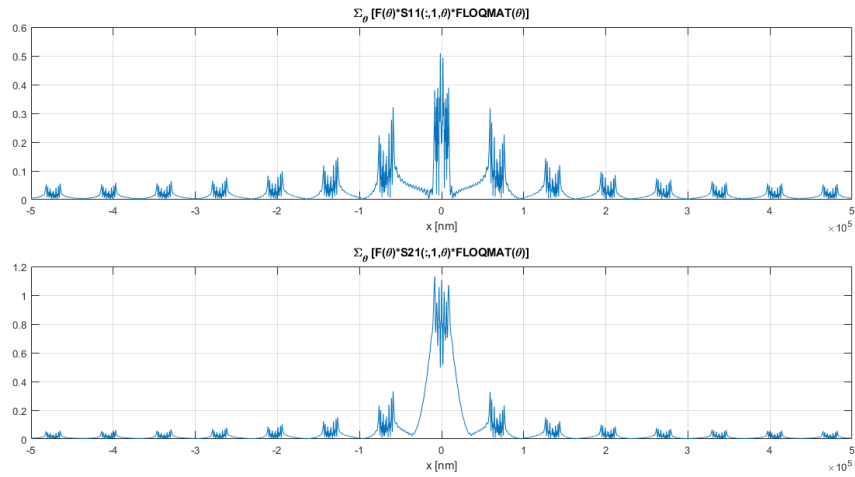


Figure 3.27: Reflected and transmitted contribution provided by the device with a cell like Figure 3.26 (bottom) with a Gaussian beam having a waist of $20 \mu m$ employed as source with normal incident at $x=0$.

Amplitude of the contributions related to the periodicity can be lowered increasing the spacers length, but the number of Floquet modes setted in the script should be increased as well in order to maintain a reasonable resolution of the reconstructed index profile. In the example made in Figure 3.28, the spacers length is $50 \mu m$.

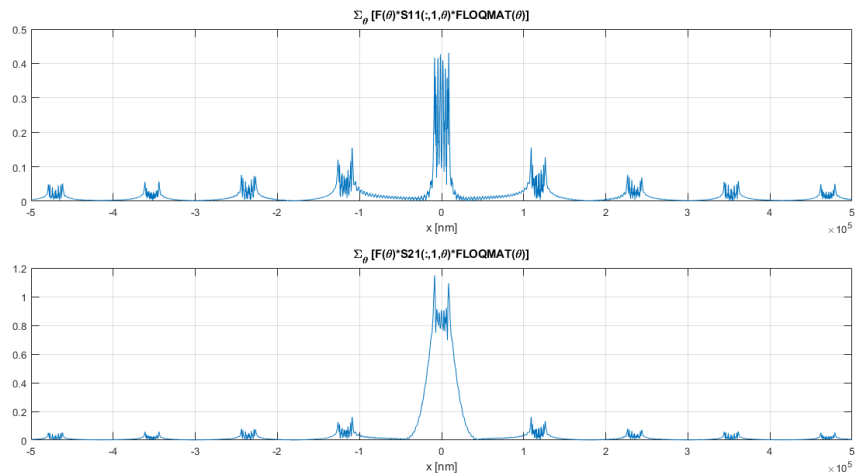


Figure 3.28: Scattered contributions with a period W of $117.6 \mu m$ and each spacer long $50 \mu m$.

Maintaining a number of selected Floquet modes equal to 151 for the plots above (which just involves a very heavy computation in MATLAB®), the reconstructed index profile degenerates into oscillation, providing a not excellent reconstruction resolution of the index profile, as seen in Figure 3.29. Clearly, it represents an issue solvable by increasing the number of modes, executing the script computation with a suitable hardware. By the way, it is important to remember that the reconstruction of dielectric profile is an operation exclusively used to check the \underline{E} matrix, i.e. if the coefficients of modal expansions correctly describe the device.

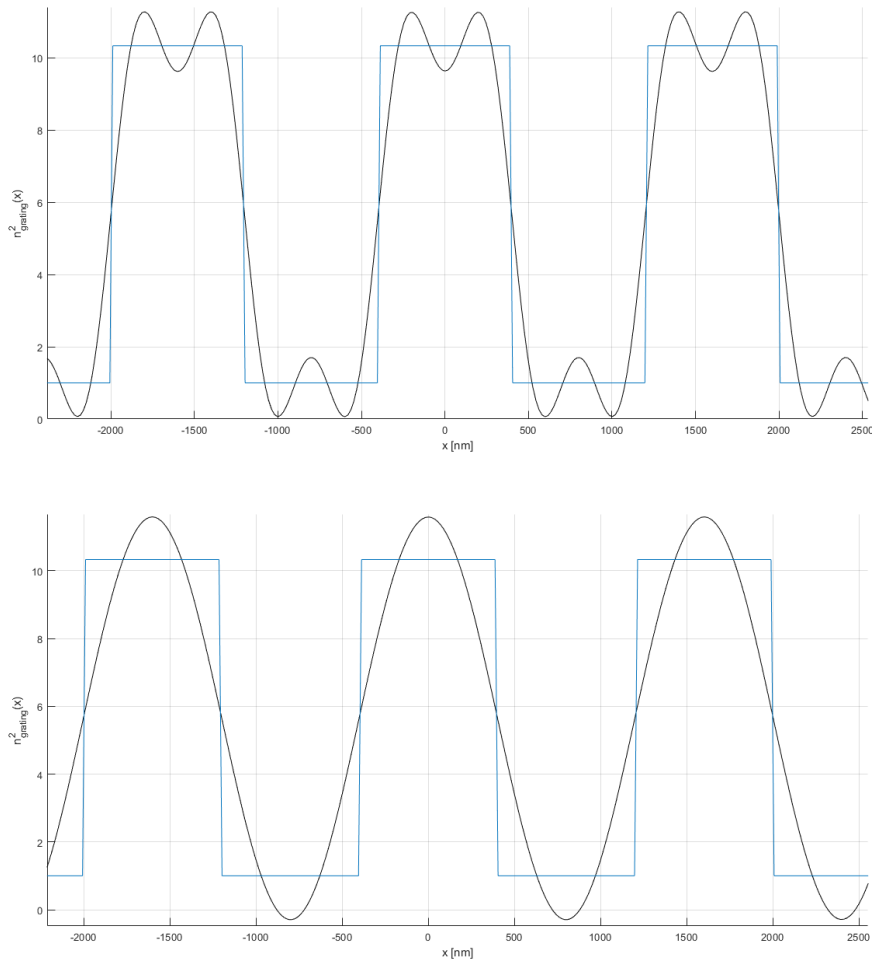


Figure 3.29: Zoomed grating zone in the case of $25\mu m$ (top) and $50\mu m$ (bottom) spacer length, with 151 Floquet modes employed in both cases.

Just for completeness, a particular case of an incident wave illuminating only the bars of a single cell has been analysed. For this purpose, a Gaussian beam with a waist four times smaller than the one used until now has been employed (i.e. $w = 5\mu m$).

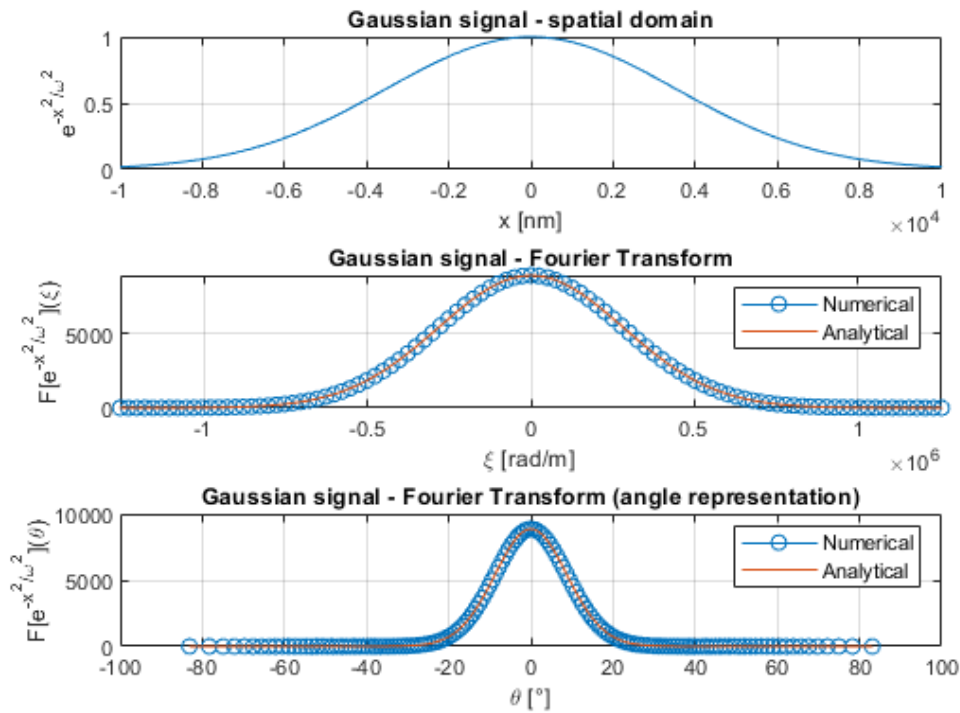


Figure 3.30: Gaussian beam with a waist of $5\mu m$ (top) and its SFT in ξ (middle) and ϑ (bottom) domains.

In this condition, maintaining the same elementary cell of Figure 3.26, the source illuminates only the "grating zone", hence it should not take into account the finiteness of the device.

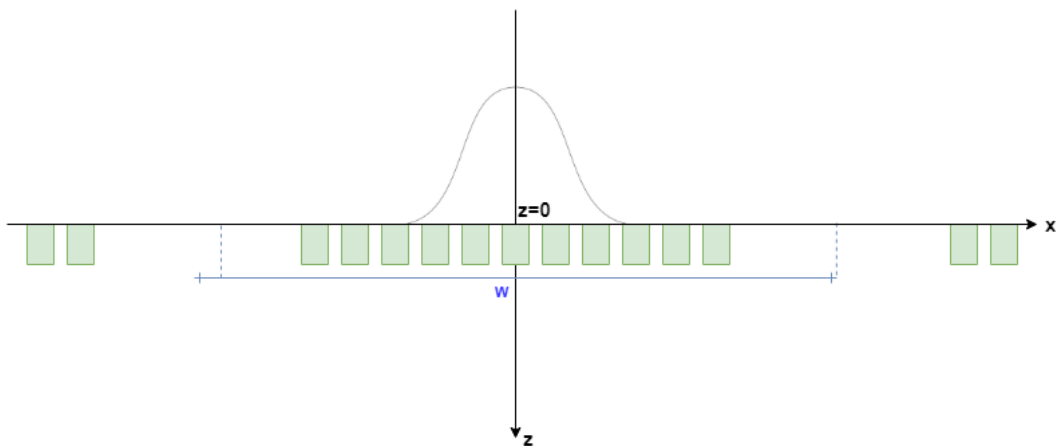


Figure 3.31: Representation of the actual condition, with the Gaussian beam illuminating only the bars-fillers zone.

3. Simulations related to the diffraction grating behaviour

What happens in the case of Figure 3.31 is that the grating should behave a bit more similar to the case of a device with infinite periodic bars, indeed the two plots just below in Figure 3.32 show two shapes at $-\frac{W}{2} < x < \frac{W}{2}$ closer to a bell curve than the case of $w = 20\mu m$.

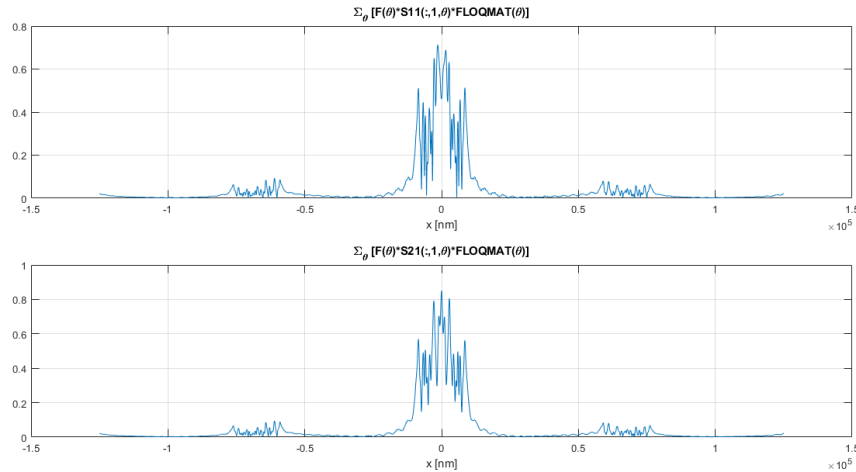


Figure 3.32: Transmitted and reflected contributions provided by the same device referring Figure 3.26 with a reduced beam waist of the bell curve.

Clearly, the effect of cell periodicity in this particular case is quite tiny (only few peaks far from the range of $x=0$ are present) since the incident contribution at the neighbour cells can be practically considered null.

Conclusions

As first step, rigorous coupled-wave analysis has been implemented as a modal method used to evaluate the scattering parameters of a diffraction grating. Floquet modes have been defined according to the fixed periodic boundary conditions, so Maxwell's Equations have been described (in the case of TE polarization and in-plane incidence assumptions) and successively projected on the Floquet modes, obtaining in this way the associated eigenvalue problem. The latter allows the achievement of the modal expansion coefficients related to the "grating waveguide" by means the eigenvectors, while the obtained eigenvalues represent the propagation constants of the grating modes.

Continuity conditions of the transversal field components at the bars-air interfaces have been enforced, therefore the so called mode-matching technique is formulated. In this way, scattering matrices related to the two junctions have been found and finally the scattering parameters related to the device are achieved by performing the cascade of aforementioned matrices. The unit cell simulating a diffraction grating of finite extent is described by properly managing the MATLAB® code related to the coefficients of modal expansions: it is composed by a grating zone and two spacing layers at its sides, aimed to simulate the device finiteness.

The design of spacers in the unit cell plays a fundamental role, indeed if they are not sufficiently long with respect to the beam waist, the scattered contributions related to the neighbour periods are not negligible. A good trade-off between the length of the spacing layers and the number of selected Floquet modes during the simulation must be done in order to achieve a good analysis (i.e. results are affected by periodicity in a negligible manner) with reasonable computation resources.

As future development of this work, a kind of improvement is represented by the introduction of "absorbing conditions" at the simulated grating boundaries. This approach could allow to reduce the length of spacing layers and therefore obtaining more precise scattering parameters of the modelled device with a smaller number of selected Floquet modes in the simulation (i.e. with less computational costs).

Bibliography

- [1] I.D. Bagbaya, "On the history of the diffraction grating" in *Soviet Physics Uspekhi*, Vol.15, p-660, Sukhumi Pedagogical Institute, 1972.
- [2] R. Porter, "The Biographical Dictionary of Scientists", Oxford University, 1994.
- [3] Dilz, RJ 2017, 'A spatial spectral domain integral equation solver for electromagnetic scattering in dielectric layered media', Doctor of Philosophy, Department of Electrical Engineering, Eindhoven.
- [4] B.A. Munk, "Jaumann and circuit analog absorbers" in *Frequency Selective Surfaces: Theory and Design*, Ch.9, Ohio State University, 2000.
- [5] A.Tibaldi, "Expressions of the Floquet mode functions" in *A Mortar Element Method for the Analysis of Electromagnetic Passive Devices*, p.157, Ph.D Thesis, Turin, 2015.
- [6] R. Orta, "Internal Report", Department of Electronics and Telecommunications, Politecnico di Torino, 2011.
- [7] R.Orta, "Cascade connection of structures" in *Lecture notes on transmission line theory*, pp.112-116, Politecnico di Torino, 2012.
- [8] G. Teschl, "Ordinary Differential Equations and Dynamical Systems". Providence: American Mathematical Society. ISBN 978-0-8218-8328-0, 2012.
- [9] R. Orta, "Waveguides" in *Lecture Notes on Passive Optical Components*, ch.8, pp.176-187, Politecnico di Torino, 2017.